Appendices to the Final Report of the
Igneous Consequences Peer Review Panel

Prepared for:
Bechtel SAIC Company LLC
Las Vegas, Nevada

Prepared by:
Emmanuel Detournay, Larry G. Mastin, J.R. Anthony Pearson,
Allan M. Rubin and Frank J. Spera

February 2003

PREFACE

The material presented herein represents Volume 2 of the Igneous Consequences Peer Review Panel Final Report (henceforth referred to as Volume 1). Volume 2 consists of the appendices to Volume 1.

The text files, tables and charts in Appendix 2 of Volume 2 are labeled according to the Chapter and Section of Volume 1 in which they first are cited. For example, text file A2.3 in this Volume 2 is keyed to Section 2.3 in Volume 1. Tables and charts are labeled sequentially and refer back to Chapters in Volume 1. For example, Table 2A is the first table in Appendix 2 and Table 2B is the second table in Appendix 2. Figures (graphs or charts) are labeled similarly, so that Figure 2B is the second figure in Appendix 2.

The Sections of Appendix 3 are numbered sequentially in the order they are cited in Chapter 3 of Volume 1. Equations in Appendix 3 are numbered sequentially within each section; unless otherwise noted, call-outs to equations refer to the Section of Appendix 3 in which the call-out appears.

TABLE OF CONTENTS

APPENDIX 2

TEXT FILES

A2.3   Estimating Magmatic Volatiles in CFVZ Basalts

The presence of amphibole, a hydroxyl-bearing phenocryst found sparsely in some CFVZ basalts, constrains the water fugacity (f_{H2O}) and the dissolved H_2O content of melt. Calculations were performed using the MELTS algorithm (Ghiorso, 1997; 1999) for the composition given in Table 2A in Appendix 2. This is an approximate calculation because activity-composition relations for Ti-bearing amphibole are not available. At 50 MPa and 1220 °C, there is no water content that causes saturation with amphibole. At 50 MPa, the "dry" liquidus temperature is 1182 °C on the QFM oxygen fugacity buffer, and the liquidus phase is olivine (Fo_{81}). The minimum chemical affinity for phase saturation of amphibole at 1220 °C and 50 MPa occurs at 2.5 wt % H_2O. At higher pressure (100 MPa and 300 MPa), the dry liquidi are 1186 °C and 1200 °C, respectively, and the minimum chemical affinity for amphibole phase saturation occurs again around 2.5 wt % H_2O. Thermochemical calculations indicate that amphibole is not stabilized at any pressure at ~ 1200 °C. Additional calculations reveal that at 100 MPa (~ 3 km depth), amphibole saturation occurs at 2.8 wt % dissolved H_2O at 1010 °C. Because the amphibole activity-composition model used in the computation does not incorporate the effects of Titania, these results cannot be considered definitive. However, based on the H_2O content of the melts at which amphibole does attain its minimum chemical affinity and allowing for the probable effects of TiO_2 on activity-composition relations, it is estimated that the maximum stability of amphibole occurs ~ 3 wt % H_2O. Multiple-phase saturation of amphibole, olivine, clinopyroxene, plagioclase and Fe-Ti oxides (magnetite crystalline solution) occurs at temperatures in the range 1025 ^{o}C to 1100 °C at 100 MPa, allowing for the role of Ti in stabilizing amphibole in a potassic trachybasalt composition. The laboratory phase equilibration experiments of Knutson and Green (1975) cited by Hill et al. (1995) provide an additional independent estimate of 2 wt % H_2O to 5 wt % H_2O for the stabilization of amphibole in an alkali basalt. This is consistent with the estimate based on MELTS Gibbs free energy minimization cited above.

A second approach for estimating volatile abundance is to examine glass and fluid inclusions within phenocrysts from the potassic trachybasalts at Lathrop Wells by quantitative IR spectroscopy. Luhr (2002) recently conducted a study and estimates H_2O and CO_2 content in the range 3 wt % to 4 wt % and several thousand parts per million (1 ppm equals 10^{-4} wt %), respectively. These values give bulk magma H_2O/CO_2 ratios (Z_{H2O}/Z_{CO2}) in the range 10 to 30.

A third method for estimating the dissolved H_2O content of CFVZ magmas is to compare the petrographically observed sequence of phenocryst crystallization with that determined by experimental phase equilibria. As an illustration, consider the crystallization sequence for composition given in Table 2A, thought to be representative of possible future eruptions at YMR. For this composition, the mineral plagioclase is the liquidus phase and remains the sole crystallizing phase for 30 ^{o}C to 50 °C below the liquidus in low-pressure (100 MPa) isobaric crystallization experiments with no added H_2O (i.e., the dry case). In contrast, this same major element composition plus 3 wt % H_2O is characterized by olivine on the liquidus and the suppression of plagioclase saturation until temperatures well below the liquidus. The order of phenocryst crystallization is a sensitive indicator of the dissolved H_2O content of the melt. In Tables 2E (Appendix 2)**,** representative results are presented of MELTS simulations showing the influence of H_2O concentration on crystallization sequence. In order to reproduce the phenocryst crystallization sequence recorded by petrographically, H_2O contents in the range 2 wt % to 4 wt % are required.

A2.5.2 Eruption Chronology of Lonquimay and Capulin Mountain

Lonquimay, Southern Chile — The volcanic history of Lonquimay volcano in the Southern Andes Volcanic Zone of Chile illustrates the importance of timescale and eruptive variability at a single volcanic center. Although Lonquimay is in a different tectonic setting (subduction zone, not extensional) and has erupted magma of different composition (basaltic andesite, not potassic trachybasalt) than post-Miocene activity in Crater Flat, its variability over time intervals from days to weeks to months to years to centuries is instructive. Lonquimay is a small, flat-topped, symmetrical polygenetic composite

stratovolcano that has erupted five times in the past 150 years (1853, 1887-1890, 1933, 1940 and 1988-1990). The most recent eruption at Lonquimay was in 1988-1990 (Moreno and Gardeweg, 1989; Smithsonian Institution, 1989; Naranjo et. al, 1992). Historical lava flows have issued from vents along the NE flank of the Lonquimay strato-cone along a SW-NE trend. All eruptions have been explosive and all have produced lava flows. However, details of each eruption vary in terms of intensity, style and volume of volcanic product. The vent of the 1853 eruption was within the central crater of the composite Lonquimay volcanic edifice. Thirty-four years later, a 19-month eruption began in June 1887. Lava issued from a radial fissure on the NE flank of Lonquimay. The dominant product of this eruption was basaltic andesitic lava of approximate volume 0.1 km^3; relatively little tephra was produced during this eruption. Small eruptions took place in 1933 and again in 1940.

The most significant eruption in the past 150 years at Lonquimay began on December 25, 1988 after a two-week period of increasing seismicity. The eruption began along a 400 m fissure trending ENE-WSW on the NE flank of the Lonquimay stratocone about 4 km from the summit crater. Vigorous tephra emission was followed several days later by substantial lava eruption feeding a block lava flow that traveled to the NNE. A 400-m high parasitic tephra cone (Navidad cone) was constructed along the fissure within the first few weeks of the eruption. Moderate ash emission and lava production continued through mid-September 1989 from Navidad cone, on the NE flank of the composite edifice. Decrease in activity at the cone began in late September and continued until late November, when the eruption intensity briefly increased. Continued ash and lava were produced in December 1989, but lava production slowed in early January 1990. The eruption ended late in January 1990, having lasted 13 months and generated 0.10 km^3 (DRE) of pyroclastic ejecta (Navidad cone plus dispersed tephra) and 0.23 km^3 (DRE) of lava, for a total volume of ~ 0.33 km^3. The fissure eruption that began Christmas day in 1988 produced lava at ~ 5 x 10^6 m^3/day averaged over the first ten days, 1.4 x 10^6 m^3/day averaged over the next 30 days, 7.5 x 10^5 m^3/day averaged over the period 31 January to 8 February, and 1.2 x 10^4 m^3/day between 17 September and late November. The rate of

tephra production is less well constrained, but about 80% of the total thickness of the tephra blanket was produced in the first ~ 50 days of the eruption (Naranjo et al., 1992). The average volumetric rate of eruption for the 1988-1990 eruptive phase at Lonquimay was ~ 0.37 km^3/year. Assuming a magma density of 2700 kg m^{-3}, the average mass flow during the 13-month eruption was 3.2 x 10^4 kg s^{-1}, within the range for typical Strombolian eruptions (10^4 kg/s to 10^6 kg/s). The eruption intensity (volume flow rate) decreased by a factor of ten in the first 100 days and by a factor of 100 in the first year.

Capulin Mountain, Raton-Clayton Volcanic Field — The Raton-Clayton Volcanic Field (RCVF), in NE New Mexico is made up of ~ 120 basaltic cinder cones (and associated lava flows) with ages in the range > 1 Ma to about 7500 years before the present. The youngest volcano in the region is Capulin Volcano, distinguished by its remarkably symmetrical cinder cone. The rim of the cone is approximately 1.7 km in circumference with a basal diameter of about 1.5 km. The cone stands 360 m high above the local base level; the central crater depth is about 125 m below the rim of the cinder cone. Capulin volcano erupted about 7500 years ago. This cinder cone represents the last stage of a period of volcanism that had begun ~ 8 Ma earlier at RCVF. The eruption began along a northwest-oriented fissure vent that centralized to form a single vent or conduit during the early part of the eruption. Powered by the conversion of PV vapor expansion work to kinetic energy, cinders were propelled by expanding gases along steep ballistic trajectories. Tephra fall deposits piled up around the vent to produce the Capulin cinder cone. Simultaneously with cinder cone growth, a sequence of four lava flows were erupted from a bocca on the NW side of the cone. The first erupted lava flowed to the SE of Capulin Mt, covering an area of several square kilometers. Following the first lava flow and rapid growth of the cinder cone, additional lava flows were emitted as mildly effusive flows from the bocca on the northwest side of the cone. Magma flowed at least partly in lava tubes, first to the south (second lava flow), then southwest (third lava flow), and finally to the north and northeast (fourth lava flow). The total area covered by lava flows is about 38 km^2. The volume of tephra making up the cone is approximately

0.7 km^3 (density ~ 1000 kg/m^3), whereas the total volume of lava is about 0.57 km^3 (density ~ 2700 kg/m^3), to give a lava/tephra mass ratio ≈ 2 for Capulin Mountain volcano.

A2.6.1 Rheology of Bubbly Magma

Once the rising magma becomes saturated with respect to vapor, it becomes important to consider the viscosity of the magmatic two-phase mixture (melt plus vapor) and not simply the viscosity of volatile-saturated melt. A key question becomes the relative motion between bubbles and melt. Are bubbles distributed homogeneously within magma traveling at the same velocity as the melt? Or will melt and vapor move upward at different velocities? Here we perform a simplified analysis of the problem.

Two cases may be differentiated. If the bubble Stokes ascent rate ($u_b = 2/9 \, g r_b^2 \Delta\rho/\eta$) is large compared to the magma ascent rate (u), bubbles will rise through ascending magma to form a vapor-rich cap. These may be removed by Darcy percolation into permeable country rock, or at least accumulate near the top of the rising dike. Alternatively, if the magma ascent rate is fast compared to bubble rise rates, the mixture can be treated as a homogeneous bubbly flow with an effective mixture viscosity. For typical parameters ($r_b \approx 5$ mm, $\Delta\rho \approx 1800$ kg/m^3, $\eta \approx 50$ Pa s and $u \approx 1$m/s), one finds u_b/u to be of the order of 10^{-3}. This implies that the melt-bubble magmatic suspension can be treated as a homogeneous bubbly flow. Naturally, at very shallow depths, when the volume fraction of vapor is close to or exceeds the critical value for magma fragmentation, u_b/u will approach unity. There is a flow regime change at this point from bubbly flow to slug flow or some other form of separated two-phase (melt-vapor) flow. The conclusion is that for bubbly flows with $\theta <\sim 0.5$, the assumption of bubbly homogeneous flow is reasonable. If the magma can be treated adequately as a homogeneous mixture, it then becomes important to determine the effect of bubbles on the shear viscosity of the magma.

There is a large literature on the shear viscosity of bubbly flows that extends from the pioneering work of G. I. Taylor (1932) to the present (Frankel and Acrivos, 1970; Stein and Spera, 1992; Bogdassarov and Dingwell, 1992; Manga et al., 1998; Lejeune et al., 1999; Martel et al., 2000; Spera and Stein, 2000; Spera, 2000; Lensky et al., 2001;

Blower et al., 2001; Pal, 2001a,b,c; Manga and Loewenberg, 2001; Rust and Manga, 2002a,b; Llewellin et al., 2002; Stein and Spera, 2002; Pal, 2003). For magmatic flows relevant to Yucca mountain, the bubble Reynolds number ($Re_b \equiv \rho G r_b^2/\eta_m$, where G, the mean shear rate, $\approx u/d$, d is the dike thickness, and η_m is the melt viscosity) is small, which means that, from the perspective of the bubble, viscous forces outweigh inertial ones. The shear viscosity of a magmatic two-phase pseudofluid mixture (η_p) is given by $\eta_p = f(\eta_m, \theta, Ca)$, where η_m is the shear viscosity of the melt (a function of pressure, temperature and composition including dissolved volatiles), θ is the volume fraction of bubbles, and Ca is the Capillary number, defined $Ca \equiv G r_b \eta_m/\sigma$, where G is a mean macroscopic shear rate, r_b is a typical bubble radius, and σ is the melt-vapor interfacial energy. It is convenient to discuss the relative viscosity (η_r), defined as the ratio of the pseudofluid (mixture) viscosity to the viscosity of the single-phase melt: $\eta_r \equiv \eta_p/\eta_m$ and so $\eta_r = g(\theta, Ca)$. There are three relevant regimes based on the magnitude of Ca. At low Ca ($Ca < 0.1$), bubbles are little deformed, and η_r is a monotonically *increasing* function of the bubble volume fraction, θ, and independent of the shear rate (or Ca number). In the dilute limit, $\eta_r = 1 + \theta$. For higher bubble fractions, there are a number of empirical relations of the form $\eta_r = h(\theta)$, where $h(\theta)$ is a monotonically increasing function of the bubble loading (θ). In this regime, the viscosity of the two-phase mixture exceeds that of the melt, and Newtonian behavior is observed. In contrast, for $0.1 < Ca < 10$, a transitional power-law regime exists such that η_r decreases as Ca increases at fixed θ. In the power law regime, the relative viscosity decreases as the volume fraction of vapor increases. Finally, for $Ca > 10$, η_r is independent of Ca and, again, a monotonically decreasing function of θ. The key factor is the magnitude of the capillary number. For application to magma beneath Yucca Mountain, $\eta_m \approx 50$ Pa s and $\sigma \approx 0.2$ N/m. For a dike 1 m thick and a magma ascent rate of 1 m/s, then, for $r_b = 1$, 3 and 10 mm, $Ca \approx 0.3$, 0.8, and 3, respectively. If the magma ascent rate is 10 m/s, then $G = 10$ s^{-1} and $Ca \approx 3$, 8 and 30, respectively. A plot of the relative viscosity of magma as a function of the volume fraction of vapor (θ) and the shear rate (or Capillary number) is presented in Figure 2B (Appendix 2).

TABLES

Table 2A *Devolatilized major element composition used in magma property calculations*

OXIDE	Percent by Mass
SiO_2	48.99
TiO_2	1.95
Al_2O_3	16.91
Fe_2O_3	1.76
FeO	8.99
MnO	0.17
MgO	5.89
CaO	8.69
Na_2O	3.57
K_2O	1.86
P_2O_5	1.23
TOTAL	100.00

Table 2B   Nomenclature for Chapter 2

Mass fraction H_2O dissolved in melt	W_{H2O}^{m}
Mass fraction CO_2 dissolved in melt	W_{CO2}^{m}
Mass fraction H_2O in vapor	W_{H2O}^{v}
Mass fraction CO_2 in vapor	W_{CO2}^{v}
Mass fraction H_2O in mixture	Z_{H2O}
Mass fraction CO_2 in mixture	Z_{CO2}
Mass fraction of vapor in mixture	ϕ
Mole fraction H_2O dissolved in melt	X_{H2O}^{m}
Mole fraction CO_2 dissolved in melt	X_{CO2}^{m}
Mole fraction H_2O in vapor	X_{H2O}^{v}
Mole fraction CO_2 in vapor	X_{CO2}^{v}
Density of CO_2 vapor (kg/m^3)	ρ_{CO2}
Density of H_2O vapor (kg/m^3)	ρ_{H2O}
Density of SO_2 vapor (kg/m^3)	ρ_{SO2}
Density of vapor (kg/m^3)	ρ_{v}
Density of melt (kg/m^3)	ρ_{m}
Density of magma (mixture) (kg/m^3)	ρ
Melt viscosity ($Pa \bullet s$)	η
Volume fraction of vapor in magma	θ
Fugacity coefficient of H_2O	χ_{H2O}
Fugacity of H_2O (Pa)	f_{H2O}
Fugacity coefficient of CO_2	χ_{CO2}
Fugacity of CO_2 (Pa)	f_{CO2}
Isobaric specific heat capacity of melt ($J/kg \bullet K$)	$c_{p,\,m}$
Isobaric specific heat capacity of H_2O vapor ($J/kg \bullet K$)	$c_{p,\,H2O}$
Isobaric specific heat capacity of CO_2 vapor ($J/kg \bullet K$)	$c_{p,\,CO2}$
Isochoric specific heat capacity of H_2O vapor ($J/kg \bullet K$)	$c_{V,\,H2O}$
Isochoric specific heat capacity of CO_2 vapor ($J/kg \bullet K$)	$c_{V,\,CO2}$
Heat capacity ratio (C_p/C_v) of vapor	k_{g}
Isobaric specific heat capacity of vapor ($J/kg \bullet K$)	$c_{p,\,v}$
Heat capacity ratio of magma	k
Mean vapor molar mass (kg/kmol)	M_{v}
constant ($J/kmol \bullet K$)	R
Vapor gas constant ($J/kmol \bullet K$)	R_{v}
Isentropic compressibility of melt (Pa^{-1})	β_{s}
Sonic velocity of melt (m/s)	c_{m}
Sonic velocity of vapor (m/s)	c_{v}
Sonic velocity of magma (m/s)	c

[TABLES 2C](#) *Magma properties versus pressure*

Fifty-four tables are presented. Properties computed are identified at the top of the table columns. Symbols and units are keyed to Table 2B. Properties are computed for magma at temperatures 1050 °C, 1150 °C and 1220 °C for H_2O/CO_2 mass ratios ($\equiv Z_{H20}/Z_{CO2}$) equal to 2, 4, 6, 10 and 20 and total volatile content ($Z_{H2O} + Z_{CO2}$) equal to 1, 2, 3 and 4 wt %. Additional tables for pure H_2O and pure CO_2 with Z_{H2O} or Z_{CO2} equal to both 4 wt % and 8 wt % are provided. All properties are computed at the following pressures: 100, 90, 80, 70, 60, 50, 40, 30, 20, 17, 14, 11, 8, 5, 2 and 0.10133 MPa.

For readers interested in seeing these tables, they will be made available in the future on the web at http://www.ymp.gov, under Technical Documents.

Those interested in obtaining a copy of these tables before they are posted may contact Thomas Rodgers at Bechtel SAIC Company LLC (1-702-295-5483).

Table 2D   Recent short-lived basaltic eruptions

Analog	Volcano Type	Magma Type	Eruption Characteristics	VEI	log V (km^3)	References
Cerro Negro	Long-lived cinder cone (150+ yrs)	Basalt, w/30% plg, 5% ol, 1% pyx phenos	Violent Strombolian eruption in 1992 produced .03 km^3 tephra over 17.5 hrs; avg. eruption rate ~ 500 m^3/s (DRE)	3	-2	Smithsonian Inst., 1992a, 1992b. Viramonte & DiScala, 1970
Parícutin, 1943-1950	Monogenetic cinder cone & lava flows	Andesite to basaltic andesite, 55-60 wt % SiO_2 (whole rock). ol$\pm$plg phenos, ol+cpx$\pm$opx microphenos.	Construction of a scoria cone ~ 420 m high, .5 km^3 lava, and ~ .7 km^3 tephra distributed over several hundred km^2. Maximum tephra column height ~ 7 km. Tephra discharge rate during early cone-building phase (2/22-26/43), ~ 40 m^3/s (= ~ 10 m^3/s DRE; Luhr & Simkin, 1993, p. 70)	3	0	Fries & Gutierrez (1952, Table 5); Segerstrom (1950, Table 22), Luhr & Simkin (1993) See Scandone (1979) for details of eruptive volume (tephra, lava and magma) versus time
Tolbachik	Fissure on a large basalt shield.	High-Al_2O_3 alkali basalt	Fissure eruptions from vents on flanks of a lava shield. Eruptions occurred at two locations (the "southern" and "northern" breakthroughs") and built cinder cones and lava flows at each location. Eruptive sequence included violent Strombolian phases and, near the end of the sequence, phreatomagmatic explosions.	3	-1	Fedotov et al., 1983; Fedotov & Markhinin, 1983.
Lonquimay, Chile, 12/25/88- 1/24/90	Fissure on a stratovolcano	Andesite to basaltic andesite (57.8-59.5 wt % SiO2)	Fissure eruption from flank vent with construction of a scoria cone ~ 300 m high, .2 km^3 lava, and ~ .23 km^3 tephra distributed over ~ 500 km^2. Maximum tephra column height ~5 km.	3	-1	Smithsonian Inst. (1989)
Izu Oshima, 11/15- 24/1986	Stratovolcano	Basalt, 53-57 % SiO2 (whole rock)	Lava fountains at summit < 1600 m high producing ~ .0018 km^3 tephra and .0019 km^3 lava. Mean eruption rate during violent phase = 1-4 m^3/s (DRE).	3	-2	Smithsonian Inst. (1986)
Heimaey, 1/23- 6/28/1973	Basaltic hot-spot volcano	Basalt; hawaiite at beginning of eruption	Eruption along a 2-km fissure that produced a cone 100 m high, ~ 0.3 km^3 lava, 0.25 km^3 tephra, max. Eruption rate ~ 10^5 kg/s in late January.	3	0	Williams & Moore (1983) Jakobsson et al. (1973)

Tables 2E Results of MELTS modeling of fractional crystallization of melt composition from Table 2A plus varying amounts of H_2O (from dry to 3 wt %) under isobaric conditions.

Note that the sequence of phenocryst crystallization depends sensitively on the dissolved H2O content of the magma. Results portrayed pictorially.

Separate plots are given for isobaric crystallization for the following cases: (10 MPa, dry), (100 MPa, dry), (100 MPa, 1 wt % H_2O), (100 MPa, 2 wt % H_2O), (100 MPa, 3 wt % H_2O). The figures show the mass fraction of each crystalline phase during isobaric fractional crystallization of the devolatilized composition listed in Table 2A plus various amounts of H_2O as a function of temperature. The mode refers to the sum of all crystalline phases present.

Liquidus Temp = 1157 ^{0}C

Melt Fraction Vs. Temp at 100 MPa and 2% H$_2$O

Legend: Olivine, Spinel, Apatite, CPX, Feldspar 1, OPX 1, Water, OPX 2, Feldspar 2, Mode

Melt Fraction vs. Temperature (^{0}C)

Liquidus Temp = 1169 ^{0}C

Melt Fraction vs. Temp at 100 MPa and 1% H$_2$O

Legend: Olivine, Feldspar 1, CPX, Spinel, Apatite, OPX, Feldspar 2, Rhm-Oxide, Water, Mode

Melt Fraction vs. Temperature (^{0}C)

Liquidus Temp = 1184 ^{0}C

Melt Fraction Dry Melt vs. Temp at 100 MPa

Legend: Feldspar, Olivine, Whitlockite, CPX 1, Spinel, CPX 2, OPX, Rhm-Oxide, Sphene, Quartz, Mode

Axes: Melt Fraction vs. Temperature (^{0}C)

Liquidus Temp = 1184 ^{0}C

Melt Fraction Dry Melt vs. Temp at 10 MPa

Legend: Feldspar, Olivine, Whitlockite, CPX, Spinel, Rhm-Oxide, Sphene, Quartz, Mode

Axes: Melt Fraction vs. Temperature (^{0}C)

FIGURES

Pliocene-Quaternary Crater Flat Basaltic Volcanism
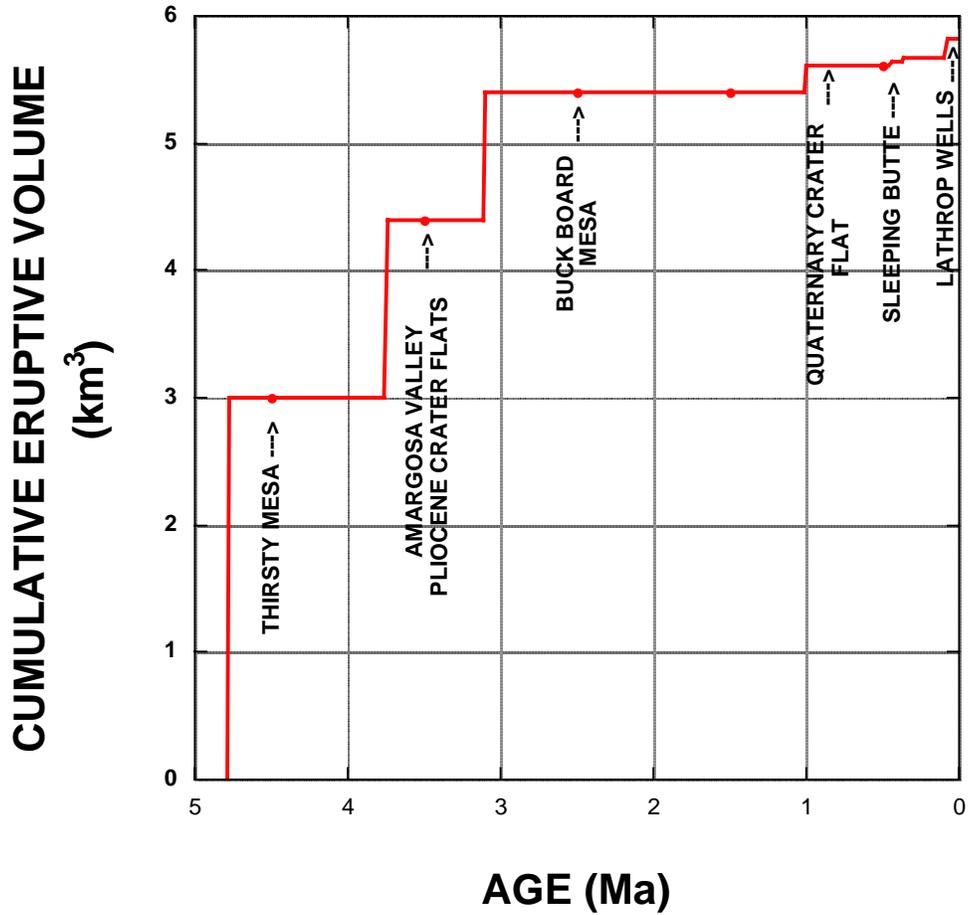
Figure 2A Cumulative volume of erupted magma versus time for post-Miocene volcanism in the Crater Flat Volcanic Zone
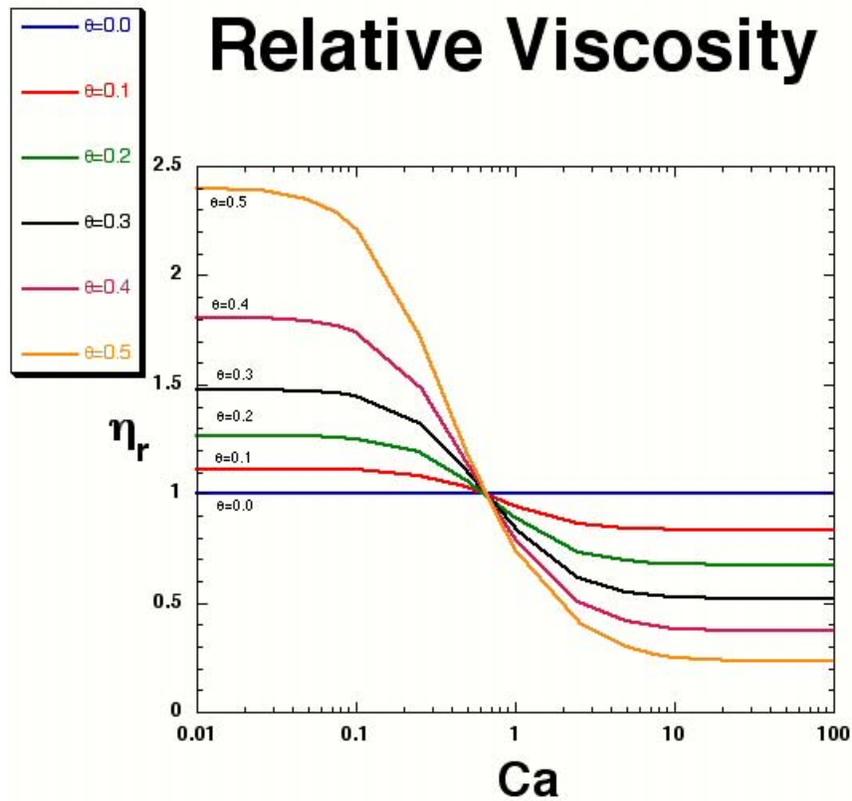
***Figure 2B Relative viscosity of magma (η_r) as a function of Capillary number (Ca) for
various volume fraction of vapor (θ) values***: The definition of both relative
viscosity and the Capillary number are noted in the text. Note that in the high
Ca regime, the shear viscosity of magma is up to a factor of 5 smaller than for
that of melt alone at the same conditions of temperature and pressure for $\theta =$
0.5. In contrast, at low Ca, the magmatic mixture is more viscous than that of
single-phase melt at the same conditions of temperature and pressure. Refer-
ences cited in Section A2.6.1, Rheology of Bubbly Magma.

REFERENCES

Blower, J. D., H. M. Mader, and S. D. R. Wilson, Coupling of viscous and diffusive controls on bubble growth during explosive volcanic eruptions, *Earth Planet. Sci. Lett*, *193*, 47-56, 2001.

Bogdassarov, N. S., and D. B. Dingwell, A rheological investigation of vesicular rhyolite, *J. Volcanol. Geotherm. Res.*, *50*, 307-322, 1992.

Doubik, P., and B. E. Hill, Magmatic and hydromagmatic conduit development during the 1975 Tolbachik eruption, Kamchatka, with implications for hazards assessment at Yucca Mountain, *J. Volcanol. Geotherm. Res.*, *91*, 43-64, 1999.

Fedotov, S. A., G. N. KKovalev, Y. E. K. Markhinin, Y. B. Slezin, A. I. Tsyurupa, N. A. Gusev, V. I. Andreyev, and V. L. Leonov, and A. A. Ovsyannikov, Chronology and features of the Southern Breakthrough of the Great Tolbachik Fissure Eruption, in *The Great Tolbachik Fissure Eruption*, edited by S. A. Fedotov, and Y. E. K. Markhinin, Cambridge University Press, Cambridge, 1983.

Fedotov, S. A., and Y. E. K. Markhinin, editors., *The Great Tolbachik Fissure Eruption*, Cambridge University Press, Cambridge, 1983.

Frankel, N. A., and A. Acrivos, The constitutive equation for a dilute emulsion, *J. Fluid Mech.*, *44*, 65-78, 1970.

Fries, C. J., and C. Gutierrez, Activity of Paricutin volcano from January 1 to June 30, 1951, *Trans. Geophys. Union*, *33*(1), 91-100, 1952.

Ghiorso, M. S., Thermodynamic models of igneous processes, *Ann. Rev. Earth Planet. Sci.*, *25*, 221-241, 1997.

Ghiorso, M. S., On the stability relations of hydrous minerals in water-undersaturated magmas, *Am. Mineralogist*, *84*, 1506-1511, 1999.

Hill, B. E., S. J. Lynton, and J. F. Luhr, Amphibole in Quaternary basalts of the Yucca Mountain region: Significance to volcanism models, in *Proceedings, Sixth Annual International High-Level Radioactive Waste Management Conference*, pp. 132-134, American Nuclear Society, La Grange Park, IL, 1995.

Jakobsson, S. P., A. Pedersen, J. G. Roensbo, and L. M. Larsen, Petrology of mugearite-hawaiite; early extrusives in the 1973 Heimaey eruption, Iceland, *Lithos*, *6*(2), 203-214, 1973.

Knutson, J., and T. H. Green, Experimental duplication of a high-pressure megacryst/cumulate assemblage in a near-saturated Hawaiite, *Contrib. Mineral. Petrol.*, *52*, 121-132, 1975.

Lejeune, A. M., Y. Bottinga, T. W. Trull, and P. Richet, Rheology of bubble-bearing magmas, *Earth Planet. Sci. Lett.*, *166*, 71-84, 1999.

Lensky, N. G., V. Lyakhovsky, and O. Mavon, Radial variations of melt viscosity around growing bubbles and gas overpressure in vesiculating magmas, *Earth Planet. Sci. Lett.*, *186*, 1-6, 2001.

Llewellin, E. W., H. M. Mader, and S. D. R. Wilson, The rheology of a bubbly liquid, *Proc. R. Soc. London A*, *458*, 987-1016, 2002.

Luhr, J. F., Melt volatile contents in basalts from Lathrop Wells and Red Cone, Yucca Mountain Region (SW Nevada): Insights from glass, *EOS*, *83*(47), F1496, 2002.

Luhr, J. F., and T. Simkin, *Parícutin: The Volcano Born in a Mexican Cornfield*, Geoscience Press, Phoenix, AZ, 1993.

Manga, M., J. Castro, K. V. Cashman, and M. Loewenberg, Rheology of bubble-bearing magmas, *J. Volcanol. Geotherm. Res.*, *87*, 15-28, 1998.

Manga, M., and M. Loewenberg, Viscosity of magmas containing highly deformable bubbles, *J. Volcanol. Geotherm. Res.*, *105*, 19-24, 2001.

Martel, C., D. B. Dingwell, O. Spieler, M. Pichavant, and M. Wilke, Fragmentation of foamed silicic melts: An experimental study, *Earth Planet. Sci. Lett.*, *178*, 47-58, 2000.

Moreno, H., and M. C. Gardeweg, La erupcion riciente en el complejo volcanica Lonquimay (Dicember 1988), Andes del sur, *Revista Geologica de Chile*, *16*, 93-117, 1989.

Naranjo, J. A., R. S. J. Sparks, M. V. Stasiuk, H. Moreno, and G. J. Ablay, Morphological, structural and textural variations in the 1988-1990 andesite lava of Lonquimay Volcano, Chile, *Geol. Mag.*, *129*, 657-678, 1992.

Pal, R., Evaluation of theoretical viscosity models for concentrated emulsions at low capillary numbers, *Chem. Eng. J.*, *81*, 15-21, 2001a.

Pal, R., Novel viscosity equations for emulsions of two immiscible liquids, *Rheol.*, *45*, 509-520, 2001b.

Pal, R., Single-parameter and two-parameter rheological equations of state for nondilute emulsions, *Ind. Eng. Chem. Res.*, *40*, 5666-5674, 2001c.

Pal, R., Rheological behavior of bubble-bearing magmas, *Earth Planet. Sci. Lett.*, *207*, 165-179, 2003.

Papale, P., Modeling of the solubility of a two-component $H_2O + CO_2$ fluid in silicate liquids, *Am. Mineralog.*, *84*, 447-492, 1999.

Rust, A. C., and M. Manga, Bubble shapes and orientations in low Re simple shear flow, *J. Colloid Interface Sci.*, *249*, 476-480, 2002a.

Rust, A. C., and M. Manga, Effects of bubble deformation on the viscosity of dilute suspensions, *J. Non-Newtonian Fluid Mech.*, *104*, 53-63, 2002b.

Scandone, R.., Effusion rate and Energy Balance of Paricutin eruption (1943-1952), Michoacan, Mexico, *J. Volcanol. Geotherm. Res.*, *6*, 45-59, 1979.

Segerstrom, K.., Erosion Studies at Parícutin Volcano, State of Michoacán, *USGS Bull*, *965A*, 1950.

Smithsonian Institution, Oshima (Japan): Lava from summit vent and 2 fissures; epicenters plot along NW-SE axis; 12,000 evacuated; summit deflated before eruption, *SEAN Bull.*, *11*(11), 3-7, 1986.

Smithsonian Institution
http://www.volcano.si.edu/gvp/world/region15/andes_c/lonquim/var.htm#bgvn_1504, 1989.

Smithsonian Institution, Details of April tephra deposits and seismicity; changes to cone; feeder dike exposed
http://www.volcano.si.edu/gvp/world/region14/nicarag/cerroneg/var_01.htm#bgvn_1704, April 1992a.

Smithsonian Institution, Strong Strombolian eruption with heavy ashfall and 28,000 evacuated, *GVN Bull.*, *17*(3), 1992b.

Spera, F. J., Physical properties of magma, in *Encyclopedia of Volcanoes, H*, edited by H. Sigurdsson, pp. 171-190, Academic Press, New York, 2000.

Spera, F. J., and D. J. Stein, Comment on "Rheology of bubble-bearing magmas" by Lejeune et al., *Earth Planet. Sci. Lett.*, *175*, 327-331, 2000.

Stein, D. J., and F. J. Spera, Rheology and microstructure of magmatic emulsions: Theory and experiments, *J. Volcanol. Geotherm. Res.*, *49*, 157-174, 1992.

Taylor, G. I., The viscosity of a fluid containing small drops of another liquid, *Proc. R. Soc. London A*, *138*, 41-48, 1932.

Viramonte, J. G., and L. DiScala, Summary of the 1968 eruption of Cerro Negro, Nicaragua, *Bull. Volcanol.*, *34*, 347-351, 1970.

Williams, R. S., and J. G. Moore, Man Against Volcano: The 1973 eruption on Haemaey, Vestmannaeyjar, Iceland, USGS
http://pubs.usgs.gov/gip/heimaey/heimaey.pdf, 1983.

APPENDIX 3

APPENDIX 3.1 GAS PRESSURE IN THE TIP CAVITY OF A DIKE PROPAGATING IN UNSATURATED ROCK

1 Introduction

When the cavity behind the tip of a propagating dike is located in an unsaturated permeable rock, the pressure of the gas in this cavity is less than the fragmentation pressure, due to leakage of gas into the country rock. The magnitude of the gas pressure is controlled by the balance between the amount of gas fed to the cavity at the fragmentation front (assumed here to coincide with the magma front) and the amount of gas bleeding off into the rock. In this appendix, we provide an estimate of this pressure using scaling arguments and back-of-the-envelope calculations. It then is shown, using reasonable values of the relevant parameters, that the gas pressure when the tip cavity is propagating in the unsaturated Yucca Mountain tuff is "low" — i.e., less than 1 MPa.

2 Gas Inflow

It can readily be argued that the total gas flow rate, Q_i, supplied at the magma front to the tip cavity is given by

$$Q_i = 2\alpha_1 w_\lambda V \tag{1}$$

where α_1 is a number of the order of 1, V is the velocity of the front (taken to be equal to the dike tip velocity), and w_λ is the half-aperture of the dike at the magma front. In reference to Appendix 3.3, w_λ can be expressed as

$$w_\lambda = \alpha_2 w_* \tag{2}$$

where α_2 is a number of order $O(10^{-1})$ or less, and w_* is the characteristic half-aperture given by

$$w_* = \left(\frac{3\eta'_m v_\infty}{\delta'} \right)^{1/2} \tag{3}$$

with η'_m denoting the viscosity of the melt, v_∞ the magma velocity at great depth, and δ' a relative unit weight. Hence,

$$Q_i = 2\alpha_1\alpha_2 \left(\frac{3\eta_m v_\infty}{\delta'} \right)^{1/2} V \tag{4}$$

3 Gas Outflow

Calculation of the gas outflow rate is based on the particular solution of the one-dimensional non-linear diffusion equation governing the evolution of gas pressure, $p(x,t)$, in the semi-infinite unsaturated permeable medium $x > 0$:

$$\frac{k}{\phi\eta_g} \frac{\partial}{\partial x}\left(p\frac{\partial p}{\partial x} \right) = \frac{\partial p}{\partial t} \tag{5}$$

with the following initial/boundary conditions: $p(x,0) = 0$, $x > 0$; $p(0,t) = p_o$, $t > 0$. (The non-linearity of (5) is a consequence of the dependence of the gas density on the pressure). In (5), ϕ denotes the rock porosity, k the rock intrinsic permeability, and η_g the gas viscosity.

The self-similar nature of this problem implies that the volumetric gas flux, $q_o(t)$, at the boundary is given by

$$q_o = \frac{\alpha_4}{2} \sqrt{\frac{\phi k p_o}{\eta_g t}} \tag{6}$$

where α_4 is a number that can be computed by solving numerically a non-linear ordinary differential equation that is deduced from (5):

$$\alpha_4 \approx 0.885 \tag{7}$$

Solution (6) can then be used to compute the volumetric flow rate, Q_o, of gas bleeding of the cavity, assumed to be propagating at the constant velocity, V, and to be filled by gas at constant pressure, p_o:

$$Q_o = \alpha_4 \sqrt{\frac{\phi k p_o V \lambda}{\eta_g}} \tag{8}$$

where λ is the length of the tip cavity.

4 Cavity Pressure Estimate

Balancing the gas mass-flow rate in and out of the cavity can be translated into the following relation between Q_o and Q_i, after recognizing that Q_i corresponds to a gas at the fragmentation pressure, p_c, and Q_o to a gas at pressure, p_o — i.e.,

$$p_o Q_o = p_c Q_i \tag{9}$$

After writing that the tip velocity, V, is of the same order as v_∞ — i.e., $V = \alpha_3 v_\infty$, with $\alpha_3 = O(1)$ — the final expression for tip cavity pressure, p_o, is deduced from (4), (8), and (9) to be

$$p_o = \beta \left(\frac{\eta_m \eta_g v_\infty^2}{\phi \delta' k \lambda} \right)^{1/3} p_c^{2/3} \tag{10}$$

where β is a number likely to be $O(10^{-1})$:

$$\beta = \left(\frac{2\alpha_1 \alpha_2}{\alpha_3} \right)^{2/3} (3\alpha_4)^{1/3} \tag{11}$$

Taking $\eta_m \approx 10^{-4}$ MPa s, $\eta_g \approx 10^{-11}$ MPa s, $v_\infty \approx 1$ m/s, $k \approx 10^{-12}$ m^2, $\lambda \approx 10^2$ m, $\delta' \approx 10^{-3}$ MN/m^3, $\phi \approx 10^{-1}$ and $p_c \approx 10^1$ MPa, we obtain $p_o \approx 1$ MPa or less.

APPENDIX 3.2   INSTABILITY OF THE DIKE TIP

The dike tip cavity is expected to respond on the (very short) timescale of rock fracture to maintain an approximate balance between the two major contributors to the stress intensity factor, *K*: the magma pressure (for the most part, an excess pressure) acting over the bulk of the dike, and the underpressure within the cavity. For a uniform cavity underpressure, Δp_λ, the (negative) contribution from the cavity increases monotonically with λ (proportionally to $-\Delta p_\lambda \lambda^{1/2}$ in the limit of small λ/l). This implies that as Δp_λ for a given dike decreases, λ increases monotonically so as to maintain $K = K_c$.

At the top of a rising dike, the pressure within the cavity, p_λ, may be taken to be quasi-uniform (at least in the context of "classical" dike propagation models with a well-defined magma front and insignificant mass in the cavity), but the dike-normal stress, σ^o decreases toward the tip at a rate $d\sigma^o/dz$. When the cavity length, λ, is small enough that $\lambda\left[d\sigma^o/dz\right] \ll \Delta p_{mf}$ where Δp_{mf} is the underpressure at the magma front, gradients in σ^o are unimportant, and the cavity underpressure may be approximated as constant. However, as the dike tip approaches the surface, the decrease in σ^o ensures that the corresponding decrease in Δp_{mf} (for fixed p_λ) and increase in λ lead to strong variations in the underpressure along the length of the cavity (decreasing toward the dike tip). Under such conditions, λ cannot increase indefinitely to offset the decreasing Δp_{mf} (to maintain $K = K_c$), because, eventually, both increasing λ and decreasing Δp_{mf} lead to an increase in *K*.

To determine when this occurs, we can write the contribution to *K* from the lag zone ($\equiv K^\lambda$) as the superposition of that due to a uniform underpressure, Δp_{mf}, and that due to an overpressure that increases linearly from zero at a distance λ behind the tip to $\lambda\left(d\sigma^o/dz\right)$ at the tip. Assuming $\lambda \ll l$, one may use the result that the stress intensity

factor due to a point force, F (per unit length), applied at a distance z behind the tip of a semi-infinite fracture is given by $K = F\left(2^{1/2}/\pi\right)z^{-1/2}$ (Tada et al., 1985). Integrating this over the cavity length, λ, yields

$$K^{\lambda} = -\frac{\sqrt{8}}{\pi}\,\Delta p_{mf}\,\lambda^{1/2} + \frac{2\sqrt{8}}{3\pi}\frac{d\sigma^{o}}{dz}\,\lambda^{3/2} \tag{1}$$

For small λ, the first term in (1) dominates, and the uniform underpressure results apply; for large λ, the second term dominates. Differentiating with respect to λ yields

$$\frac{dK^{\lambda}}{d\lambda} \approx \left(-0.45\,\Delta p_{mf} + 0.9\,\lambda\,\frac{d\sigma^{o}}{dz}\right)\lambda^{-1/2} \tag{2}$$

Setting (2) to zero shows that K^{λ} reaches a minimum for $\lambda = \Delta p_{mf}/2\left(d\sigma^{o}/dz\right)$. This means that as the dike tip shallows and λ increases from small values, K^{λ} first decreases but then increases when the underpressure at the tip, Δp_{tip}, is $0.5\,\Delta p_{mf}$ — that is, long before the tip develops an overpressure. (Even though the net suction force within the lag zone increases with λ beyond this critical value, K^{λ} decreases in magnitude because the Green's function for K is heavily weighted toward those stresses applied very near the tip, and Δp_{tip} decreases as λ increases.)

The implication of Eq. (2) for rising dikes is that there is a strong tendency for the tip to go unstable once λ grows to the point that $\Delta p_{tip} \approx 0.5\,\Delta p_{mf}$. This view is somewhat simplistic in that (in addition to using a small λ/l approximation and neglecting the free surface) it neglects the changing pressure distribution behind the magma front as λ increases and how that affects K. Nevertheless, preliminary results from the full numerical calculations shown in Chapter 3 indicate that $\Delta p_{tip} \approx 0.5\,\Delta p_{mf}$ is a reasonably good rule-of-thumb for instability, suggesting that the changing pressure distribution behind the magma front does not have a large influence on K.

Equation (2) is not enough to determine the depth at which a given dike tip will tend to go unstable; for this, an additional relation is needed. A rough — but nonetheless, useful — estimate can be obtained from a global balance for the stress intensity factor, *K*, which, for conceptual purposes, may be thought of as having contributions from three sources:

$$K = K^{\Delta P} + K^{visc} + K^{\lambda} = K_c \qquad (3)$$

where $K^{\Delta P}$ (positive) is the contribution that would result from a constant excess pressure, ΔP, acting all the way to the tip of a dike of length scale, *l*; K^{visc} (negative) is the contribution from the drop in excess pressure due to viscous flow up to the magma front; and K^{λ} (negative) is the contribution from the tip cavity. We assume $K^{\Delta p} \gg K_c$, so (3) may be approximated as $K^{\Delta P} + K^{visc} + K^{\lambda} \approx 0$. For $\lambda \ll l$, K^{visc} exceeds K^{λ}, and the dominant balance is between $K^{\Delta P}$ and K^{visc}. However, when the magma is buoyant all the way to the dike tip and the tip is approaching instability (as for the examples shown in Chapter 3), λ is large enough that $K^{visc} < K^{\lambda}$. In this case, we may write $K^{\lambda} = -\alpha K^{\Delta P}$, where α is an unknown coefficient less than (but near to) unity.

$K^{\Delta P}$ is given by $\Delta P l^{1/2}$, where the relevant length scale, *l*, is the lesser of (1) (half) the lateral extent of the dike, or (2) the vertical extent of the region over which the excess pressure is substantially larger than that at great depth. To determine K^{λ} at instability, substitute $\Delta p_{mf} / 2$ for $\lambda \left(d\sigma^o / dz \right)$ in (1) to yield

$$K^{\lambda} \approx -0.6 \, \Delta p_{mf} \, \lambda^{1/2} \approx -1.2 \, \frac{d\sigma}{dz} \lambda^{3/2} \approx 0.4 \, \Delta p_{mf}^{3/2} \left(\frac{d\sigma^o}{dz} \right)^{-1/2} \qquad (4)$$

Setting $K^{\lambda} = -\alpha \, \Delta P l^{1/2}$ yields (at instability),

$$\lambda \approx \left[0.8 \, \alpha \, \Delta P l^{1/2} \left(\frac{d\sigma^o}{dz} \right)^{-1} \right]^{2/3} \quad ; \quad \Delta p_{mf} \approx \left[2.4 \, \alpha \, \Delta P l^{1/2} \left(\frac{d\sigma}{dz} \right)^{1/2} \right]^{2/3} \qquad (5)$$

To compare the estimate in (5) to the results of Figure 3-4, we can substitute $\alpha \approx 1$, $\Delta P \approx 2.5$ MPa (an average over the length scale of 2 km), $l \approx 2$ km (half the lateral extent), and $\left(d\sigma^o / dz \right) = 12$ MPa/km to find $\lambda = 380$ m and $\Delta p_{mf} \approx 9.5$ MPa at instability. These values are reasonably close to the numerical values of $\lambda = 320$ m and $\Delta p_{mf} \approx 6.8$ MPa. (Closer agreement would be had for $\alpha = 0.7$, a plausible value.) A greater exploration of parameter space by the numerical models may be required to see if this rough agreement holds generally. Perhaps the most important point is that, despite the simplicity of this elastic analysis, which ignores all coupling to the fluid flow (except through the unknown constant α, which should be close to 1), Eq. (5) seems sufficient to show that, for dike lengths of the order of 1 km and excess pressures of a few MPa, the tip cavity length at instability is of the order of hundreds of meters —not tens of meters or less.

Two processes conceivably could reduce considerably the length of the tip cavity at instability. First, if inelastic deformation becomes distributed over a wide region as the dike tip approaches the surface (comparable to the tip depth, for example), rather than being concentrated only along the plane of the dike, this effectively imparts a compression to the cavity that will lessen the distance from the magma front to the dike tip. In a crude sense, this may be thought of as increasing the rock fracture toughness, K_c, to values orders of magnitude larger than those measured from laboratory tests. Second, if the dike is filled with magma with a low enough bubble content to be effectively "negatively buoyant", $\Delta P l^{1/2}$ may grossly overestimate $K^{\Delta P}$, so that K^{λ} (and, hence, λ) at instability will be considerably less. Note that, in the latter case, the tendency for lateral propagation of the dike is much stronger than the tendency for vertical propagation (see below).

Observations

Few fissure eruptions have been observed from the time the dike tip first breached the surface. Duffield et al. (1982) report that during the 1971 eruption in the Southwest Rift

of Kilauea, a line of lava fountains moved downrift at about 0.15 m/s, ahead of which new ground cracks opened and pre-existing cracks widened. "Then in rapid succession, volcanic fume combined with condensing steam from vaporized ground water (?) issued from the cracks, clots of molten lava were ejected in Strombolian fashion to heights of a few meters, dense dark fume billowed forth, and finally lava fountaining began." The paper is not quantitative about the timing, but Duffield (personal communication, 2002) states "The sequence of action immediately before lava fountaining probably lasted no more than a minute or two at a fixed site. It may have been less than a minute." Because vertical flow rates are likely to have been less than horizontal flow rates for this dike, the tip may have been no more than 10 m beneath the surface when the cracks appeared. However, for low-gas eruptions in Hawaii, the magma may be effectively negatively buoyant nearly to the surface; in this case, the crack tip can be stabilized with a lag zone so short that the instability discussed above does not occur until much shallower (because of the underpressure over much of the upper portion of the dike; see, for example, Rubin, 1990; Lister and Kerr, 1991).

Observations more pertinent to the YMR may come from the onset of the eruption of Parícutin in 1943 (Foshag and Gonzales, 1956). As is discussed in Appendix 3.4, the parent dike may have been halted at depth by freezing near the tip. After about 2 weeks of seismic activity, a fissure ~ 50 m long and ~ 5 cm wide opened up, followed about 8 hours later by vigorous fountaining thought to mark the arrival of a robust magma supply to the surface. Very little magmatic material came out of the crack initially, and what came out did so quite gently; thus, a reasonable interpretation is that the crack was driven not by a high-pressure gas phase, but by gradual inflation of the dike at depth. (The same gradual inflation could have been responsible for the stress increase driving the seismicity.) The depth of the magma front at the time of fissure formation is unknown. Three-dimensional boundary element calculations for a subsurface dike with a fixed (rectangular) geometry, but gradually increasing (uniform) magma pressure and an atmospheric-pressure cavity show that, as expected, the tip cavity gradually increases in height and is tallest above the dike midpoint. Instability occurs when this tallest portion

is roughly half the distance to the surface, consistent with the conclusion following from Eq. (2). The maximum thickness of the first crack to breach the surface is only a very small fraction of the maximum dike thickness, so 5 cm is not an unreasonable value for this scenario. The strike length of this unstable crack appears to be roughly equal to the depth of the magma front (as long as the lateral extent of the dike is much greater), suggesting a minimum depth of 50 m for the dike tip at Parícutin. However, it is quite likely that the full extent of the (thin) surface fissure was obscured by having to propagate through near-surface soils, placing the actual dike tip deeper.

APPENDIX 3.3 MATHEMATICAL MODEL OF PROPAGATING DIKE WITH COMPRESSIBLE HOMOGENEOUS FLOW

1 Introduction

Mathematical models of dikes that can be found in the literature involve only incompressible magma; see Lister and Kerr (1991), Rubin (1995a) and Rubin (2003) for reviews. The expected H_2O and CO_2 content of the magma considered for a hypothetical intrusion at Yucca Mountain implies that volatiles will exsolve from the magma during its ascent (see Chapters 2 and 3). This appendix summarizes some of the efforts expended by the Panel to modify classical dike models to account for the exsolution process as well as for the fragmentation of the magma when the magma pressure drops below a critical pressure p_c (a function of the magma composition). The new models remain rudimentary, however, and are proposed here only as a first step toward the incorporation of the complex physics that takes place during ascent of a magma with a high volatile content.

Consider first the classical problem of a vertical dike propagating in a semi-infinite elastic medium and driven by an *incompressible* Newtonian magma, which is injected at the base of the dike at a constant volumetric rate, q_∞. Several assumptions are introduced to simplify this problem:

(1) plane strain conditions apply;

(2) the magma is injected at infinity;

(3) the dike propagates continuously in mobile equilibrium; and

(4) lubrication theory and linear elastic fracture mechanics are applicable.

The complete formulation of this problem relies on equations from elasticity and lubrication theories, on a fracture propagation criterion from linear elastic fracture mechanics, and on boundary conditions at the inlet and at the tip of the fracture. Within this description, several parameters are used to characterize the rock, the magma, the far-field

horizontal stress, and the boundary conditions. The material constants needed for the rock are Young's modulus (E), Poisson's ratio (v), toughness (K_{Ilc}) and density (ρ_r), while the relevant constants for the magma are the dynamic viscosity (η) and the density (ρ_f). For convenience, we introduce the reduced constants

$$E^{'} = \frac{E}{1-v^2}, \quad K^{'} = 4\left(\frac{2}{\pi}\right)^{1/2} K_{Ic}, \quad \eta^{'} = 12\eta \tag{1}$$

(While $E^{'}$ is the plane strain modulus, the new parameters ($K^{'}$, $\eta^{'}$) are introduced simply to unclutter the governing equations from numerical factors.). The horizontal stress field, σ_o, is assumed to vary with depth z according to

$$\sigma_o = \sigma_c + \chi\rho_r g z \tag{2}$$

where σ_c is a constant stress, g is the acceleration of gravity, and χ is a number that is typically in the range $0.3 \leq \chi \leq 1$. Finally, the boundary conditions at infinity correspond to a constant injection flow rate, q_∞. The mathematical model can be used to compute the fracture half-aperture, $w(z,t)$, the magma pressure, $p_f(z,t)$, and the flow rate, $q(z,t)$ as a function of depth z and time t, as well as to study the dependence of the solution on the problem parameters. (Note that q is taken positive when directed upward, in the opposite direction to the z-axis.)

A dike model, which accounts in an approximate manner for the presence of dissolved volatiles in the magma, can be constructed by modifying classical dike models to include the compressibility of the magma due to the gas bubbles in the continuity equation, a thermodynamic relationship between the bubble volume fraction and the magma pressure, and the condition at which magma fragments. Two cases are considered, corresponding to the dike tip propagating in either an impermeable or permeable rock.

Case 1: Tip in Impermeable Rock and a Slowly Growing Cavity — Three regions can be distinguished along the dike:

    (1)   an incompressible flow region at large depth;

    (2)   a homogeneous compressible flow region characterized by an increasing bubble fraction with decreasing depth and same (average) velocity for the gas and the liquid phase (This region is bounded above by the magma front $z_m(t)$.); and

    (3)   a tip cavity between the magma front, $z_m(t)$, and the dike tip, $h(t)$. (The tip cavity is filled with vapors at the fragmentation pressure, p_c. Thus, the magma front is characterized by the critical bubble volume fraction, θ_c, at which magma fragments.)

Case 2: Tip in Permeable Rock or a Rapidly Growing Cavity — Four regions can be distinguished along the dike:

    (1) an incompressible flow region at great depth, as in Case 1;

    (2) a homogeneous compressible flow region, as in Case 1. (This region is bounded above by the fragmentation front, $z_c(t)$, where the gas phase becomes continuous.);

    (3) a complex flow region between the fragmentation front, $z_c(t)$, and the moving magma front, $z_m(t)$. (This is a region where several poorly understood mechanisms take place, such as channeling of gas in the magma/bubble mixture, and bleeding of the gas into the host rock.); and

    (4) a tip cavity between the magma front, $z_m(t)$, and the dike tip, $h(t)$. (The pressure in the cavity is assumed to be at uniform pressure, p_{fo}, which is less than p_c, because gas is bleeding off in the rock. In the

calculations reported in Figure 3-5 of the main text, the tip vapor pressure p_{fo} was set to zero in view of the large permeability of the Yucca Mountain tuff.)

This appendix concerns the two models (Model 1 and 2) introduced in Chapter 3. In Sections 2 and 3, we focus on Model 2 under the more general Case 2 conditions. (Indeed, if $p_{fo} = p_c$, the magma front, $z_m(t)$, and the fragmentation front, $z_c(t)$, coincide.) This model makes dramatic simplifications for the complex flow region by assuming that the magma completely degasses in this region over a distance small compared to the its length, either by bleeding gas into the country rock and/or via high-velocity gas channels that transfer gas from the fragmentation front to the magma front. Under these conditions, the fragmentation front can be viewed as a sharp front separating magma at the critical bubble fraction, θ_c, from pure melt. Thus, this model is characterized by a discontinuity of the bubble fraction, although the pressure remains continuous. Under these assumptions, the magma flow in the region between the magma front and the fragmentation front simplifies to an incompressible Poiseuille flow. In Section 4, we summarize the features of Model 1 that differ from those of Model 2. The most salient difference is in the treatment of the region between the fragmentation front and the dike tip.

2 Mathematical Formulation for Model 2

2.1 Elasticity Equation

The elastic relation between the fluid pressure, $p_f(z,t)$, and the fracture aperture, $w(z,t)$, is expressed by a singular integral equation (Hills et al., 1996):

$$p_f(z,t) - \sigma_o(z) = 2E' \int_{h(t)}^{\infty} M(z,s) \frac{\partial w(s,t)}{\partial s} ds \tag{3}$$

where $M(z,s)$ is an elastic kernel that accounts for the presence of a free surface:

$$M(z,s) = M_\infty(z,s) - \frac{1}{4\pi(z+s)} - \frac{2s}{4\pi(z+s)^2} + \frac{4s^2}{4\pi(z+s)^3} \tag{4}$$

with $M_\infty(z,s)$ denoting the Cauchy singular kernel for the infinite plane,

$$M_\infty(z,s) = \frac{1}{4\pi(z-s)} \tag{5}$$

We will refer to $p_f - \sigma_o$ as the net pressure, p.

2.2 Poiseuille Law

According to lubrication theory, the equation governing the flow of a Newtonian fluid within the fracture is given by (Batchelor, 1967):

$$q = \frac{8w^3}{\eta'}\left(\frac{\partial p_f}{\partial z} - \rho_f g\right) \tag{6}$$

where ρ_f is the magma density, and g is the acceleration of gravity.

Writing η' and ρ_f in terms of the viscosity of the melt (η'_m) and the density of the melt (ρ_{fm}),

$$\eta' = \eta'_m\, m(\theta, \dot{\gamma}) \tag{7}$$

$$\rho_f = \rho_{fm}(1-\theta) \tag{8}$$

where θ denotes the volume fraction of the gas bubbles and $\dot{\gamma}$ the shear strain rate of the magma. Note that in a first approximation, $m = 1$.

2.3 Constitutive Equation for the Bubble Volume Fraction

The bubble volume fraction, θ, is a function of the absolute magma pressure, p_f, which depends on the composition of the magma. Here, we assume that the constitutive equation is of the form

$$\frac{p_f - p_c}{p_o} = \left(\frac{\theta_c - \theta}{\theta}\right)^{\alpha} \tag{9}$$

where p_o is a reference pressure, p_c is the fragmentation pressure, θ_c is the critical bubble volume fraction (at which magma fragments), and α is a positive number. Note that this form of the constitutive equation implies that the magma becomes incompressible at great depth (i.e., at great pressure); thus, there is no formal need to distinguish between regions 1 and 2, as done in the Introduction.

2.4 Fluid Mass Balance

By assuming incompressibility of the pure melt, the local mass balance can be expressed as

$$2\frac{\partial w}{\partial t} - \frac{\partial q}{\partial z} - \frac{1}{1-\theta}\left(2w\frac{\partial \theta}{\partial t} - q\frac{\partial \theta}{\partial z}\right) = 0 \tag{10}$$

In the pure melt region, this equation reduces to

$$2\frac{\partial w}{\partial t} - \frac{\partial q}{\partial z} = 0 \tag{11}$$

2.5 Propagation Criterion

The propagation criterion imposes the asymptotic form of w at the tip (Rice, 1968):

$$w = \frac{K'}{2E'}(z-h)^{1/2}, \quad z \to h \tag{12}$$

This criterion obviously implies that $w = 0$ at $z = h$.

2.6 Condition in the Lag Zone

$$p_f = p_{fo}, \quad h(t) \le z < z_m(t) \tag{13}$$

2.7 Condition at the Magma Front

At the magma front, $z = z_m(t)$, the fluid pressure is the gas pressure, p_{fo}, in the lag zone, and the velocity of the front corresponds to the average magma velocity at the front. Hence,

$$p_f = p_{fo}, \quad \frac{dz_m}{dt} = \frac{4w^2}{\eta} \left(\frac{\partial p_f}{\partial z} - \rho_{fm} g \right) \quad \text{at} \quad z = z_m(t) \tag{14}$$

where the position of the fluid front, z_m, is given by

$$z_m = h + \ell \tag{15}$$

with ℓ being the length of the tip cavity.

2.8 Condition at the Fragmentation Front

At the fragmentation front, $z = z_c(t)$, the magma pressure is continuous and equal to the fragmentation pressure, p_c. Under the assumption that the magma degasses completely at the fragmentation front, both θ and the flow rate, q, are discontinuous at $z = z_c(t)$. Conservation of the melt across the front implies that

$$2\theta_c w v_c = q_- - (1 - \theta_c) q_+ \quad \text{at} \quad z = z_c(t) \tag{16}$$

where q_+ and q_- denote, respectively, the volumetric flow rate upstream and down-stream of the front, and v_c is the velocity of the fragmentation front:

$$v_c = -\frac{dz_c}{dt} \tag{17}$$

2.9 Condition at Infinity

The condition at infinity corresponds to a constant injection rate, q_∞:

$$q = q_\infty \quad \text{at} \quad z = \infty \tag{18}$$

It can be shown that this condition corresponds to a constant mean velocity, v_∞, at infinity.

The set consisting of the elasticity equation (3), Poiseuille law (6), fluid continuity (10), propagation criterion (12), conditions at the fronts (14) and (16), and conditions at infinity (18) form a complete system for determining $w(z,t)$, $p_f(z,t)$, $h(t)$, $z_c(t)$, $z_m(t)$, and $\ell(t)$, starting from known values of these quantities at an initial time, t_0.

3 Scaling (Model 2)

Scaling this problem hinges on introducing the following characteristic quantities: length, ℓ_*; time, t_*; width, w_*; pressure, p_*; and flow rate, q_*. Then we define the dimensionless depth, ζ, and time, τ, as

$$\zeta = z/\ell_* \quad \text{and} \quad \tau = t/t_* \tag{19}$$

the dimensionless crack opening, $\Omega(\zeta,\tau)$, the net pressure $\Pi(\zeta,\tau)$, and flow rate, $\Psi(\zeta,\tau)$, as

$$\Omega = 2w/w_*, \Pi = p/p_*, \Psi = q/q_* \tag{20}$$

as well as the depth of the dike tip, $\psi(\tau)$, the length of the tip cavity, $\lambda(\tau)$, and the position of the magma front, $\varphi_m(\tau)$, and the fragmentation front, $\varphi_c(\tau)$,

$$\psi = h/\ell_*, \lambda = \ell/\ell_*, \varphi_m = z_m/\ell_*, \varphi_c = z_c/\ell_* \tag{21}$$

Recall that $\varphi_m = \psi + \lambda$. The characteristic quantities ℓ_*, t_*, w_*, p_*, and q_* will be identified below.

Using (19)-(21), the system of equations governing $\Omega(\zeta,\tau)$, $\Pi(\zeta,\tau)$, $\Psi(\zeta,\tau)$, $\psi(\tau)$, $\varphi_c(\tau)$ and $\varphi_m(\tau)$ become as shown below.

Elasticity Equation

$$\Pi = G_e \int_\psi^\infty M(\zeta, s) \frac{\partial \Omega}{\partial s} ds \tag{22}$$

Poiseuille Law

$$G_m \Psi = \frac{\Omega^3}{m} \left[\frac{\partial \Pi}{\partial \zeta} + G_\gamma - (1 - G_t)\,\theta \right] \tag{23}$$

Constitutive Equation for Bubble Volume Fraction

$$\Pi - \Pi_c = G_b \left(\frac{\theta_c - \theta}{\theta} \right)^\alpha \quad \text{with} \quad \Pi_c = G_s - G_t\,\zeta \tag{24}$$

Fluid Continuity

$$G_w \frac{\partial \Omega}{\partial \tau} - \frac{\partial \Psi}{\partial \zeta} - \frac{1}{1-\theta} \left(\Omega \frac{\partial \theta}{\partial \tau} - \Psi \frac{\partial \theta}{\partial \zeta} \right) = 0 \tag{25}$$

Fracture Propagation Criterion

$$\Omega = G_k \left(\zeta - \psi \right)^{1/2} \quad \text{as} \quad \zeta \to \psi \tag{26}$$

Boundary Condition in the Tip Cavity

$$\Pi = -(G_p + G_t \zeta), \ \psi < \zeta \le \varphi_m \tag{27}$$

Boundary Condition at the Magma Front

$$G_m G_w \dot{\varphi}_m = -\frac{\Omega^2}{m} \left[\frac{\partial \Pi}{\partial \zeta} + G_\gamma \right] \quad \text{at} \ \zeta = \varphi_m \tag{28}$$

Interface Condition at the Fragmentation Front

$$\Pi = \Pi_c, \quad -G_w \theta_c \Omega \, \dot{\phi}_c = \Psi_- - (1 - \theta_c)\Psi_+ \quad \text{at} \quad \zeta = \varphi_c \tag{29}$$

Boundary Condition at Infinity

$$\Psi = G_q \quad \text{as} \quad \zeta \to \infty \tag{30}$$

The eight dimensionless groups G_e, G_m, G_γ, G_w, G_q, G_k, G_t, G_p are defined as follows:

$$G_e = \frac{2E'w_*}{p_*\ell_*}, G_m = \frac{\eta' q_* \ell_*}{8w_*^3 p_*}, G_\gamma = \frac{\delta' \ell_*}{p_*}, G_w = \frac{2w_* \ell_*}{t_* q_*}, G_q = \frac{q}{q_*} \tag{31}$$

$$G_k = \frac{K'\ell_*^{1/2}}{2E'w_*}, G_p = \frac{\sigma_c - p_{fo}}{p_*}, G_t = \frac{\chi \rho_r g \ell_*}{p_*}, G_b = \frac{p_o}{p_*}, G_s = \frac{p_c - \sigma_c}{p_*} \tag{32}$$

where $\delta' = (\chi \rho_r - \rho_{fm})g$. The particular scaling used in this problem is selected by imposing that the five dimensionless groups in (31) are all equal to one,

$$G_e = G_m = G_\gamma = G_w = G_q = 1 \tag{33}$$

so as to define the five characteristic quantities ℓ_*, t_*, w_*, p_*, and q_*, which are then given by

$$\ell_* = \left(\frac{\eta'_m E'^3 q_\infty}{\delta'^4}\right)^{1/6}, w_* = \left(\frac{\eta'_m q_\infty}{8\delta'}\right)^{1/3}, p_* = \left(\eta'_m E'^3 \delta'^2 q_\infty\right)^{1/6} \tag{34}$$

$$t_* = \left(\frac{\eta'_m E'}{\delta'^2 q_\infty}\right)^{1/2}, q_* = q_\infty \tag{35}$$

Also, the three remaining groups are renamed as

$$G_k \equiv \kappa, \ G_p \equiv \sigma, \ G_t \equiv \gamma, \ G_b \equiv \beta, \ G_s \equiv \phi \tag{36}$$

where κ will be referred to as the toughness, σ as a reference stress, γ as the relative host rock density, β as the reference pressure (for the thermodynamic relationship

between the bubble volume fraction and the magma pressure), and ϕ as the fragmenta-tion pressure.

$$\kappa = K' \left(\frac{1}{\eta'_m E'^3 q_\infty} \right)^{1/4}, \quad \sigma = \frac{\sigma_c - p_{fo}}{\left[\eta'_m E'^3 \delta'^2 q_\infty \right]^{1/6}}, \quad \gamma = \frac{\chi \rho_r}{\chi \rho_r - \rho_{fm}} \tag{37}$$

$$\beta = \frac{p_o}{\left[\eta'_m E'^3 \delta'^2 q_\infty \right]^{1/6}}, \quad \phi = \frac{p_c - \sigma_c}{\left[\eta'_m E'^3 \delta'^2 q_\infty \right]^{1/6}} \tag{38}$$

This scaling is an extension of the scaling used by Lister (1990) for the self-similar propagation of a dike to the time-dependent case with compressible magma. Note that this scaling collapses if $\delta' = 0$. (For example, $\delta' = 0$ if $\chi = 1$ and $\rho_r = \rho_{fm}$.) In that case, an appropriate scaling would correspond to

$$G_e = G_m = G_t = G_w = G_q = 1 \tag{39}$$

when $G_\gamma = 0$, from which new expressions for ℓ_*, t_*, w_*, p_*, and q_* can be derived easily.

3.1 Dimensionless Formulation

In summary, the set of governing equations can be written as

$$\Pi = \int_\psi^\infty M(\zeta, s) \frac{\partial \Omega}{\partial s} ds, \quad \Psi = \frac{\Omega^3}{m} \left[\frac{\partial \Pi}{\partial \zeta} + 1 - (1 - \gamma) \theta \right] \tag{40}$$

$$\Pi - \phi + \gamma \zeta = \beta \left(\frac{\theta_c - \theta}{\theta} \right)^\alpha, \quad \frac{\partial \Omega}{\partial \tau} - \frac{\partial \Psi}{\partial \zeta} - \frac{1}{1 - \theta} \left(\Omega \frac{\partial \theta}{\partial \tau} - \Psi \frac{\partial \theta}{\partial \zeta} \right) = 0 \tag{41}$$

with the propagation criterion and the conditions in the lag zone, at the fluid and frag-mentation fronts and at infinity given by

$$\Omega = \kappa (\zeta - \psi)^{1/2}, \zeta \to \psi \tag{42}$$

$$\Pi = -\left(\sigma + \gamma\zeta\right), \quad \psi < \zeta \le \varphi_m \tag{43}$$

$$\dot{\varphi}_m = -\frac{\Omega^2}{m}\left[\frac{\partial\Pi}{\partial\zeta} + \gamma\right] \quad \text{at} \quad \zeta = \varphi_m \tag{44}$$

$$\Pi = \phi - \gamma\zeta, \quad \theta_c\Omega\,\dot{\varphi}_c = \Psi_- - (1-\theta_c)\Psi_+ \quad \text{at} \quad \zeta = \varphi_c \tag{45}$$

$$\Psi = 1, \zeta \to \infty \tag{46}$$

The system of equations (40)-(45) is closed in the sense that it can be used to determine the solution $F(\zeta,\tau;\kappa,\gamma,\sigma,\alpha,\beta,\phi)$, where $F = \{\Omega, \Pi, \Psi, \theta, \psi, \varphi_c, \varphi_m\}$, given a suitable set of initial conditions.

It can be shown readily (as already recognized by Lister (1990) for the self-similar case) that the solution behaves at infinity as

$$\Omega = 1, \Pi = \frac{1}{4\pi\zeta}, \zeta \to \infty \tag{47}$$

Hence, the average magma velocity is $\Upsilon \equiv \Psi/\Omega = 1$ at $\zeta = \infty$. In dimensional terms, the average fluid velocity at infinity, v_∞, is given as

$$v_\infty = \left(\frac{\delta' q_\infty^2}{\eta_m'}\right)^{1/3} \tag{48}$$

It is convenient to formulate the boundary conditions at infinity in terms of v_∞ rather than q_∞. Hence, the characteristic quantities can be formulated as follows:

$$\ell_* = \left(\frac{\eta_m' E'^2 v_\infty}{\delta'^3}\right)^{1/4}, \quad w_* = \left(\frac{\eta_m' v_\infty}{4\delta'}\right)^{1/2}, \quad p_* = \left(\eta_m' E'^2 \delta' v_\infty\right)^{1/4}$$
$$t_* = \frac{\ell_*}{v_\infty}, \quad q_* = 2v_\infty w_* \tag{49}$$

and

$$\kappa = K' \left(\frac{\delta'}{\eta_m'^3 E'^6 v_\infty^6} \right)^{1/8}, \quad \sigma = \frac{\sigma_c - p_{fo}}{\left(\eta_m' E'^2 \delta' v_\infty \right)^{1/4}} \tag{50}$$

Further details on Model 2, as well as a presentation of the numerical implementation of this model, are discussed by Detournay and Savitski (2003).

4 Formulation for Model 1

4.1 *Elasticity*

Rather than relating spatial gradients of the dike thickness to stresses (Eq. 3) using the 2D elastic Green's functions of Eq. (4), Figure 3-4 uses the 3D Green's functions for a dike of finite lateral extent. The equations are analytic but cumbersome to write; they are given by Okada (1992) and were implemented using the program DIS3D (Erickson, 1986). Because of the added complexity of these Green's functions, the effect of the free surface is not included. "The resulting calculation is only "pseudo 3-D" in that the dike thickness is constant along strike, the host rock stress and magma pressure are computed only along the dike centerline, and fluid flow equation is solved only for 1-D vertical flow along that centerline." Ideally, one would like to model a fully 3D elastic (planar) dike with 2D flow in that plane and compute the lateral extent of the dike as a function of depth and time; however, in the absence of access to such a code, it was deemed useful to explore the influence of a finite lateral extent in this approximate fashion.

For a semi-infinite 2D dike of infinite lateral extent (e.g., Figure 3-5), the relevant length scale, l_* (Eq. 34) is determined by the flux boundary condition at infinity and can be deduced from the following argument. Far from the dike tip, the excess pressure approaches zero, because any finite pressure applied over a sufficiently large height would generate thicknesses (and hence fluxes) too large to be supplied by the source. This means that the pressure gradient for flow is simply the "effective" magma buoyancy, $\delta' = \left(\chi \rho_r - \rho_{fm} \right) g$. (For scaling purposes, we phrase this discussion in terms of the bubble-free magma density, ρ_{fm}). Given this pressure gradient, the dike thickness far from the tip adjusts itself to the source flux and is given by w_* in Eq. (34). Because the local excess pressure is ~ 0, this thickness is produced by the finite excess pressure produced over the length scale, l_*, near the tip. The dimensional estimate of l_* comes from the elasticity equation,

$$w_* / l_* \approx 2 \, p_* / E' \approx 2 \, \delta' l_* / E' \text{, or}$$

$$l_* = \left(\frac{w_* E'}{2\,\delta'} \right)^{1/2}$$

(51)

In deriving (51), we equate the bulk excess pressure in the dike nose (of the order of p_*) with $\delta' l_*$; this would be appropriate for a static magma column of height l_*. In practice, the dike widening associated with the local excess pressure and the dependence of velocity on the thickness squared make this a useful dimensional estimate despite the fact that the magma is flowing.

Introduction of a finite lateral extent obviously introduces an additional length scale, defined here as half the lateral extent, l_1. The finite extent implies that the dike cannot be held open at infinity by an excess pressure applied only near the tip. Instead of the excess pressure asymptotically approaching zero at infinity, for a constant flux, it approaches a constant value, Δp^∞, given by

$$\frac{w_*}{l_1} = \frac{2\,\Delta p^\infty}{E'}$$

(52)

This Δp^∞ implies another natural length scale, l_2, given by

$$\delta' l \;= \Delta p^\infty \Rightarrow l_2 = \Delta p^\infty / \delta'$$

(53)

— that is, l_2 is the vertical length required for the effective magma buoyancy to generate a pressure equal to that at the dike source (or, equivalently, that required to generate the thickness that can accommodate the source flux). Combining (52) and (53) and comparing with (51) shows that l_*, l_1 and l_2 are related by $l_* = \left(l_1 l_2 \right)^{1/2}$.

For a dike of finite lateral extent, the most relevant length scale is the smaller of l_* and l_1. When $l_* \ll l_1$, by analogy with the infinite-strike-length dike, the dike thickness at infinity can be reached elastically by an excess pressure, $\delta' l_*$, applied over a distance that is small compared to l_1. The dike develops an elastic nose with a vertical extent less than

l_1 and an excess pressure that is many times Δp^{∞} (compared to an infinite amount larger, for l_1 = infinity). In contrast, for $l_* \gg l_1$, pressures much larger than Δp^{∞} do not develop. Figure 3-4 shows something of a transition between these states. For the adopted parameters, $l_* = l_1$. For the deeper dike, vesiculation is not yet significant, and excess pressures modestly larger than Δp^{∞} are distributed over a vertical extent larger than l_1. Thus, l_1 is the length limiting the dike thickness. For the shallower dike, vesiculation and the effective magma buoyancy have increased to the point that the "effective" l_* (one based on the local effective buoyancy) would be less than l_1, such that the dike is beginning to develop an elastic nose smaller than l_1 (seen most clearly in the excess pressure profile).

4.2 Poiseuille Flow

This section is identical to Section 2.2 of Appendix 3.3.

4.3 Bubble Volume Fraction

To simplify the expression for the bubble fraction in the implicit finite-difference numerical scheme, the bubble fraction as a function of pressure is given not by Eq. (9), but is assumed to vary linearly from a value of 1 at zero pressure to 0 at a pressure P_{exs} dependent upon the volatile content of the magma. This linear dependence on pressure accurately describes the magma at bubble fractions larger than about 0.3, but not at small bubble fractions (e.g., Figure 2-1c).

The magma bubble fraction controls both the magma buoyancy and the magma compressibility. At low bubble fractions, a given pressure change corresponds to only a small fractional volume change, and the most important influence is on magma buoyancy (particularly for small δ'). The adopted expression for bubble fraction does a rather poor job of capturing buoyancy variations as a function of pressure in this low bubble-fraction range. At large bubble fractions, a given pressure change corresponds to a large fractional volume change, and the effective magma buoyancy changes only slightly. (The buoyancy begins to "saturate" because it cannot exceed the "effective" host rock density, $\chi \rho_r$). This is where the adopted expression for bubble fraction does a good job of

mimicking magma. Because we are most interested in the behavior near a shallow dike tip where large bubble fractions are present over an extended region and where the adopted expression for the bubble fraction is fairly accurate, the adopted expression is believed to be an adequate approximation.

4.4 Fluid Mass Balance

This section is identical to Section 2.4 of Appendix 3.3.

4.5 Propagation Criterion

Because of the added complexity of the elastic Green's functions for a dike of finite lateral extent, the grid spacing is fixed in space to be 0.005 l_1 (e.g., a 10 m spacing for a half-length of 2 km). To satisfy approximately a propagation criterion of $K = 0$, the equations of elasticity, Poiseuille flow, bubble volume fraction, fluid mass balance, condition in the lag zone, and condition at the magma front are first satisfied for a "trial" lag zone length that remains unchanged from the prior timestep. (This is carried out in an implicit sense in a reference frame moving with the magma front.) If, for this trial length, the tensile stress perturbation at a distance of 1/2 the grid spacing ahead of the dike tip exceeds the ambient confining pressure, the trial calculation is redone with a cavity length larger by one grid spacing. This iterative procedure is repeated until the tensile stress perturbation is less than the ambient compression (or instability occurs, corresponding to the lack of such a stable state). In principle, it seems that it should be possible to satisfy all the relevant equations (except the tip propagation criterion) for any "trial" value of the lag length. In practice, once the cavity length increased by about 25% relative to the last stable length illustrated in Figure 3-4, no solutions could be found.

4.6 Condition in the Lag Zone

As in Section 2.6 of Appendix 3.3, the lag zone is assumed to be entirely gas-filled with a uniform pressure that is continuous with the pressure at the magma front. Unlike Section

2.6, this pressure is allowed to vary with dike ascent according to the prescription in the following section.

4.7   Condition at the Magma Front

Following the discussion of Chapter 3, Section 3.2.3 of the main Report, it is assumed that, nominally (that is, for a slowly growing and impermeable cavity; the "Case 1" of Section 1 of Appendix 3.3), the pressure in the cavity equals a fixed magma "fragmentation" pressure. Under such conditions, which might be applicable when the dike tip is located well below the water table and is far from instability, gas flux across the magma front is plausibly non-explosive. In addition, because the cavity pressure is hypothesized to be constant, only that fraction of the gas required to feed the growing cavity actually crosses the magma front. To account for this gas flux, the condition at the magma front becomes

$$v_{mf} = \langle v \rangle - \frac{1}{w} \frac{dV_{cavity}}{dt} \tag{54}$$

where v_{mf} is the velocity of the magma front, V_{cavity} is the volume of the tip cavity determined from the equations of elasticity, and $\langle v \rangle$ and w are the average flow velocity and dike half-thickness (evaluated here at the magma front), respectively.

If the cavity grows sufficiently rapidly, it can not be maintained at constant pressure by the available bubble fraction at the magma front. For a given $\langle v \rangle$ and bubble fraction θ, there is a maximum potential gas flux across the magma front that is estimated below.

Because of the no-slip boundary condition at the dike wall, magma near the dike wall moves more slowly than the magma front, while that near the dike center moves more rapidly than the magma front. Magma that reaches the magma front has the opportunity to degas partially or completely as it turns toward the wall and forms the slower-moving return flow ("return flow" in the reference frame of the moving magma front). In the following derivation, we ignore all complexities related to 2D flow and phase separation

near the magma front. We assume that the parabolic flow profile, applicable a few dike thicknesses behind the magma front in the case of incompressible flow, is also applicable at the magma front in the compressible-flow case. The gas flux into the cavity can then be determined by equating the dense liquid volume of the undegassed magma that crosses the magma front, with the dense liquid volume of the partially degassed magma moving slower than the magma front.

From the parabolic flow assumption, the downstream flow velocity, v, as a function of cross-stream distance, y, from the dike center is given by

$$v = \frac{3}{2}\left[1 - \left(\frac{y}{w}\right)^2\right]\langle v \rangle \tag{55}$$

In the absence of phase separation, the magma front velocity is equal to the average flow velocity at the magma front. With gas escape into the tip cavity, the magma front velocity is less. The cross-stream coordinate, y', which separates undegassed from partially degassed magma, is also the coordinate at which the local flow velocity equals the magma front velocity, v_{mf}. Writing y' for y when v equals v_{mf} in (55) yields

$$\frac{v_{mf}}{\langle v \rangle} = \frac{3}{2}\left[1 - \left(\frac{y'}{w}\right)^2\right] \tag{56}$$

Mass balance dictates that the dense liquid fraction of the magma that reaches the magma front equals the dense liquid fraction of the return flow that moves more slowly than the magma front. In equation form,

$$(1-\theta)\int_0^{y'}\left(\frac{3}{2}\left[1 - \left(\frac{y}{w}\right)^2\right]\langle v \rangle - v_{mf}\right)dy = (1-\alpha)\int_{y'}^{w}\left(v_{mf} - \frac{3}{2}\left[1 - \left(\frac{y}{w}\right)^2\right]\langle v \rangle\right)dy \tag{57}$$

The integral from 0 to y' on the left gives the total volume of material crossing the magma front using the parabolic flow approximation; $(1-\theta)$ represents the dense liquid fraction, and θ the bubble fraction. The integral from y' to w on the left gives the total

volume of the return flow; $(1-\alpha)$ represents the dense liquid fraction, and α the bubble fraction of the degassed magma. Dividing both sides of (57) by $\langle v \rangle$, substituting (56) for $v_{mf}/\langle v \rangle$, and integrating leads to a cubic equation for y'/w in terms of θ and α:

$$-\theta \left(\frac{y'}{w}\right)^3 + \frac{3}{2}\left(\frac{y'}{w}\right)^2 - \frac{1}{2} + \alpha \left[\left(\frac{y'}{w}\right)^3 - \frac{3}{2}\left(\frac{y'}{w}\right)^2 + \frac{1}{2} \right] = 0 \tag{58}$$

For complete degassing ($\alpha = 0$), the volume flux of gas, q_{in}, across the magma front into the tip cavity is equal to the integral on the left side of (57) multiplied by the bubble fraction, θ; integration leads to

$$q_{in} = 2 \langle v \rangle \, w \, \theta \left(\frac{y'}{w}\right)^3 \tag{59}$$

If the cavity grows sufficiently slowly that dV_{cavity}/dt is less than this maximum value, then (54) can be satisfied with a constant (time-invariant) cavity pressure. (We neglect density increases due to cooling here.) However, as instability of the dike tip is approached, dV_{cavity}/dt begins to exceed this value, and the cavity pressure drops in response so that q_{in} increases. In this case, instead of (54), the condition at the magma front becomes

$$v_{mf} = \langle v \rangle - \frac{1}{w} \frac{dV_{cavity}}{dt} - \frac{V_{cavity}}{wp} \frac{dp}{dt} \tag{60}$$

where p is the (no longer constant) pressure evaluated at the magma front (also the cavity pressure), and the last term on the right accounts for expansion of the gas already present in the cavity.

Physically, one expects that as the cavity pressure drops farther and farther below the fragmentation pressure, "fragmentation" becomes more and more explosive, with perhaps a larger and larger fraction of the magmatic material being accelerated downstream into the tip cavity. For small pressure differences, fragmentation may be only mildly explo-

sive, and the assumption of a uniform-pressure gas-filled cavity, with all the magma re-maining behind the magma front, may not be a bad approximation.

4.8 Condition at the Fragmentation Front

Following the above prescription, there is no "fragmentation front" in the sense of mag-matic liquids or solids being accelerated in the downstream direction at that point. In this prescription, the cavity remains 100% gas, and all the degassed magma becomes part of the "return flow" moving more slowly than the magma front. A more general prescrip-tion would account for the magmatic material that gets accelerated into the "cavity" as the cavity pressure drops progressively farther below the fragmentation pressure. In practice, in Figure 3-4, the cavity became unstable when the pressure dropped from the nominal "fragmentation" pressure of 10 MPa (corresponding roughly to 2.5 weight per-cent H_2O) to only 9.7 MPa.

4.9 Condition at Infinity

This section is identical to Section 2.9 of Appendix 3.3.

4.10 Dimensionless Groups

The 5 dimensionless parameters needed to completely specify the calculations (with the values used in Figure 3-4 given in brackets) are:

$$\left(\Delta p^{\infty}/l_1\right)/\delta'$$ [1.0]: excess pressure at infinity divided by the dike half-length, normalized by the effective buoyancy of dense magma

$$p_{exs}/\Delta p^{\infty}$$ [18.5]: gas exsolution pressure, normalized by excess pres-sure at infinity

$$\rho_{fm} / \left(\chi \rho_r - \rho_{fm} \right)$$

[23.0]: density of dense magma, normalized by effective density contrast between rock and dense magma

$$\chi \rho_r g / \left(\Delta p^{\infty} / l_1 \right)$$

[12.0]: gradient of normal stress in host rock, normalized by excess pressure at infinity divided by the dike half-length

$$p_c / \Delta p^{\infty}$$

[5.0]: nominal fragmentation pressure, normalized by excess pressure at infinity

To translate to parameters appropriate for the YMR, one can choose (for example) $l_1 = 2$ km (half the dike lateral extent), $\Delta p^{\infty} = 2$ MPa (excess pressure at infinity), $\delta' = 1$ MPa/km (effective buoyancy of dense magma), $\Delta p^{\infty} = 37$ MPa (gas exsolution pressure in the linear approximation; appropriate for ~ 2.5 wt % H_2O), $\chi \rho_r g = 12$ MPa/km (rate of increase of dike-normal stress with depth), $\rho_{fm} g = 11.5$ MPa/km (Note that an unreasonably low density of gas-free magma is required for the dike to ascend if a uniform host rock stress gradient of only 12 MPa/km is assumed; see Rubin (2003) for further discussion), and $p_c = 10$ MPa (nominal fragmentation pressure, appropriate for ~ 2.5 wt % H_2O). The value of E' does not enter the calculations but is required to translate dimensionless to dimensional thicknesses; for $l_1 = 2$ km and $\Delta p^{\infty} = 2$ MPa, the full thickness at infinity would be 1 m for $E' = 16$ GPa.

5 Summary

Except for modest differences (presence/absence of the free surface; infinite/finite lateral extent of the dike; magma equation of state), Models 1 and 2 treat Case 1 dikes (cavity pressure equals fragmentation pressure) in the same manner. The main difference arises when the cavity pressure is less than the nominal fragmentation pressure (Case 2). In Model 2, all the magma reaching the fragmentation front passes through the front and "clogs" the cavity; the great simplification is that it is assumed that the cavity is so permeable that all the gas exits the cavity in a narrow zone at the fragmentation front, while the remaining magmatic material can be described adequately by Poiseuille flow. In Model 1, all the magma reaching the fragmentation front is assumed to become part of the "return flow" moving more slowly than the magma front, and the great simplification is that the "cavity" can be treated as a pure gas phase at constant pressure. In reality, once fragmentation occurs, the equations governing the region between the fragmentation front and the dike tip should include inertial terms (as in more "standard" conduit flow calculations; e.g., Melnik, 2000), channeling of gas through magma accelerated across the fragmentation front, gas leak-off into the host rock, and perhaps a strain-rate-dependent fragmentation criterion.

The goals of such calculations should be to understand the likely properties (pressure, length) of the tip cavities of gas-rich dikes that may impinge upon the YMR. Despite the fact that Models 1 and 2 are quite rudimentary compared to what is desired, they represent a step in the direction of addressing these questions. As the models are quite distinct, their similarities (dimensionless tip cavity size at instability, increase in magma flow velocity and hence gas flux into the tip cavity at the fragmentation front) can be used, in conjunction with future modeling efforts, to place more confident bounds on these properties.

APPENDIX 3.4 MAGMA FREEZING

1 General

Magma freezing (and subsequent remelting, for sufficiently robust flows) has been incorporated into some models of dike propagation, often at the expense of simplifying other aspects of the problem such as neglecting elasticity (Delaney and Pollard, 1982; Bruce and Huppert, 1990; Rubin, 1995b; Lister, 1994; Lister and Dellar, 1996; Fialko and Rubin, 1998). Thermal problems of this sort are resistant to simple analytical solutions because they vary critically in space as well as time (e.g., the local flow velocity can be greatly influenced by solidification far downstream, the dominant mechanisms of heat transfer can vary along the flow, etc.).

Independent of the details of the approximations adopted by numerical calculations, one can imagine two time periods at which freezing might be important: shortly after the passage of the magma front, which could retard propagation by restricting flow near the (already thin) tip; and long after the passage of the magma front, when freezing may be responsible for shutting off the flow completely. Two mechanisms for freezing are available: conduction out the dike walls, which should be important over most of the dike ascent path and which for much of the duration of the flow is restricted to a thin boundary layer near the dike walls, and raising of the liquidus temperature due to volatile exsolution, which might always be important at the dike tip but which becomes important over a larger and larger portion of the dike as the tip shallows (which affects magma across the entire dike thickness). Mechanisms for retarding freezing are viscous dissipation and (for constant volatile concentration) decreasing the liquidus temperature with decreasing pressure, as well as latent heat release.

Existing models of freezing during magma flow generally assume the magma to be a single-component system with a unique freezing temperature. For the purposes of Appendix 3.4, this approximation is adequate. Relevant thermal parameters are the latent heat of fusion, L (~ 350 kJ/kg for basalt; see Table 1-2), thermal diffusivity, κ

(~ 0.3 x 10^{-6} m^2/s; an average of the magma and host rock values of ~ 0.2 x 10^{-6} m^2/s and ~ 0.4 x 10^{-6} m^2/s, respectively), heat capacity, c (~ 1.1 kJ/kg $^{\circ}$C), magma temperature minus host rock temperature, T_m - T_r , and magma temperature minus the solidus temperature, T_m - T_s . The assumption of a well-defined freezing temperature implies that all solidification or melting occurs at a moving boundary at the edge of the flow.

2 Conduction

Immediately upon coming into contact with cold rock, heat flow is dominated by conduction, and (assuming planar geometry) a 1D heat diffusion equation is adequate for determining the thickness of the chilled margin, δ:

$$\delta = 2\,\lambda_d\,\sqrt{\kappa t} \tag{1}$$

with λ_d given by (Carslaw and Jaeger, Ch. 11, Eq. 33):

$$\frac{\sqrt{\pi}L}{c\left(T_m - T_r\right)} = \frac{1}{\lambda_d}\left[\frac{e^{-\lambda_d^2}}{1 + erf\left(\lambda_d\right)} - \frac{T_m - T_s}{T_m - T_r}\frac{e^{-\lambda_d^2}}{erfc\left(\lambda_d\right)}\right] \tag{2}$$

(For cases where the thermal properties of the magma and host rock differ, see the original equation.) Thus, for early times, the chilled margin grows as the square-root of time. While this equation can (and should) be solved for λ_d numerically, as a temporary approximation, we can make use of the fact that, for basalts, $L > c\left(T_m - T_s\right)$ (more heat carried in as latent heat than as excess temperature), we can drop the second term in the brackets in (2) and use Figure 4-36 of Turcotte and Schubert (1982) to find λ_d ~ 0.7 (given the thermal parameters in the preceding paragraph and $T_m - T_r = 1000^{\circ}$). Thus, from (1), the frozen margin grows as $\delta \approx 1.0$ x 10^{-3} $t^{1/2}$ in mks units (e.g., 1 cm in 100 s, and 30 cm in 10^5 s or 1 day). As δ approaches the dike half-thickness, w , this simple expression underestimates δ because it ignores the cooling influence of the opposite dike

wall. However, neglect of advection of heat by the magma (discussed below) is a more significant deficiency.

This cooling time basically is consistent with observations of the eruption of ~ m-wide dikes in Iceland and Hawaii, which tend to localize from a "curtain-of-fire" to one or more quasi-cylindrical conduits ("plugs") in a matter of hours to days. In principle, this localization can be thermal or mechanical in origin. Based on observations of eroded dikes and associated plugs, Delaney and Pollard (1981) inferred that mechanical breccia-tion and erosion of the dike wall rock is responsible, often initiating at overlapping dike segments with small offsets. Once this mechanical widening occurs, the plugs can cap-ture a larger share of the flow and are much more resistant to heat loss than the uneroded portions of the dike. Thermal instabilities are also a potential cause, although it seems that such instabilities do not initiate until the dike has already cooled substantially (Lister and Dellar, 1996). It is not yet clear that such instabilities can stave off solidification in the absence of a "jump-start" by mechanical erosion. Given the potential for mechanical erosion and overlapping en-echelon dike segmentation at a dike/drift intersection, it seems reasonable (and conservative) to assume that plugs in a dike that has intersected one or more drifts form preferentially so as to include this intersection along their path.

3 Propagation Distance

Flow of a hot fluid through an initially cold channel of half-thickness w can be divided into an upstream region, where most of the heat resides in the fluid, and a downstream region, where most of this heat has been lost by conduction to the solid (Delaney and Pollard, 1982). The dividing region is known as the "thermal entrance length", l_{TE}, and its estimate is essentially the product of the flow velocity, u, and the conductive cooling time:

$$l_{TE} = u \, w^2 / 4 \, \lambda_d^2 \, \kappa \qquad\qquad (3)$$

For the above conductive cooling time of $t = 10^6 \, w^2$ (in mks units) and a flow velocity of 1 m/s, a 1 m dike ($w = 50$ cm) has an estimated thermal entrance length of 250 km. However, Delaney and Pollard (1982) showed that if the dike maintained a constant pressure gradient, accounting for how growth of the chilled margin slows the flow reduces the estimated thermal entrance length by a factor of 10, to 25 km for the parameters adopted above.

While this estimate does not account for the increased host rock temperature at depth or the reduction in liquidus temperature with decreasing pressure (at least until gas exsolution occurs), it does illustrate that meter-wide mantle-derived dikes are not immune from the effects of freezing prior to or shortly after the onset of eruption. Although more work is needed before a clear understanding is at hand, it is worth noting that for basalts coming from about 1 GPa pressure (the moho), the increase in liquidus temperature upon devolatilization roughly is comparable to (perhaps slightly smaller than) the decrease in liquidus temperature due to depressurization. The liquidus temperature increase increases with total volatile content; the magnitude of the liquidus temperature decrease increases with ascent distance. For this reason, it would be useful to have an idea of the depth of origin of the dike (independent of the depth of the source region, which is thought to be ~ 100 km in this region — e.g., Wang et al., 2002).

Freezing near the tip of the parent dike at shallow depth (shallow by coincidence or due to volatile exsolution) might help explain observations of the onset of the eruption of Paricutin. If the tip froze, but buoyant magma (or bubbles) at depth continued to ascend, the resulting widening of the dike and associated pressure increase could explain the weeks of earthquake activity prior to eruption and the ultimate propagation of a crack (observed size 50 m by 5 cm) to the surface (also see Appendix 3.2). Following crack propagation to the surface, the eruption gradually evolved from gentle to violent over a period of ~ 8 hours. Because unstable crack propagation to the surface would be accompanied by stresses tending to widen and perhaps fracture the frozen magma front, a plausible explanation for the gradually increasing violence of eruption would be the local and gradual mechanical erosion of the frozen magma front by escaping gases. The onset

of the eruption also marked the cessation of earthquake activity, consistent with a lack of continued pressure increase due to increased magma storage or bubble ascent at depth.

4 Freezing During Dike Initiation

The thermal entrance length, l_{TE}, is also a useful concept when considering the role of freezing in a secondary or dog-leg dike emanating from a drift. For a dike growing from a source of constant excess pressure, ΔP, under plane-strain conditions, both the dike thickness and propagation velocity increase linearly with dike length, l, as $w \approx \left(2\,\Delta P / E'\right) l$ and $u \approx 0.25\left(1/3\,\eta\right) w^2 \left(\Delta P / l\right)$ (here, E' is $E/\left(1-v^2\right)$, where E is the Young's modulus, v is Poisson's ratio, η is the magma viscosity, the expression for u assumes no retardation due to freezing, and the leading coefficient of ~ 0.25 comes from numerical calculations — e.g., Rubin, 1995a). Taking the product of propagation ($\sim$ flow) velocity and cooling time and substituting for w yields

$$l_{TE} = \frac{1}{3}\,\frac{1}{\lambda_d^2 \kappa \eta}\,\Delta P \left(\frac{\Delta P}{E'}\right)^4 l^3 \qquad (4)$$

Thus, the ratio of the thermal entrance length to dike length increases as the dike length squared, and short dikes are always longer than the thermal entrance length and can only grow under special circumstances. The critical dike length, l_c, such that $l_{TE} > l$ for $l > l_c$, is from (4):

$$l_c = \lambda_d \left(\frac{E'}{\Delta P}\right)^2 \left(\frac{3\kappa \eta}{\Delta P}\right)^{1/2} \qquad (5)$$

For $\eta = 50$ Pa s (We assume the magma to be considerably degassed at this point; see Figure 2-1e of the main Report.), $\Delta P = 1$ MPa (a reasonable value for a secondary dike emanating from a drift, because the magma pressure is limited by that at the intersection of the drift and the parent dike), $E' = 2$ GPa ($\sim 1/7$ the in-situ value at the decimeter scale, yielding a thickness:length aspect ratio of 10^{-3}), we find $l_c = 20$ m. In fact, for the given

parameters, this is an underestimate of l_c , because the estimate of propagation velocity (1) neglects the retarding influence of the growing chilled margin, and (2) assumes 1D flow from a linear source, rather than radial flow from a 5-m diameter conduit. Each of these would slow the flow relative to the values assumed here. On the other hand, it should be noted that the dependence of l_c on $\Delta P^{5/2}$ means that only a two-fold increase in ΔP would reduce the above estimate to ~ 3.5 m (although a two-fold increase in E' would essentially reverse this change).

In one sense, the precise value of l_c is irrelevant: No magmatic dike can start in a zero-thickness crack in rock below the solidus temperature. However, the value is relevant in that the host rock at the source may approach the magma temperature, or the initial crack may have a non-zero thickness; these are the "special circumstances" alluded to above.

♦ Dikes emanating from mantle source rocks or a shallow plug can survive thermally if above-solidus temperatures extend more than l_c from the point of initiation. In the case of growth from a drift, preheating by a substantial fraction of the magma temperature over a distance of 20 m is not reasonable.

♦ For the parameters as above, the critical crack has a full thickness $2w$ of several centimeters 10 m from the drift. This is too large to be present in the drift prior to magma arrival, but, if a gas-filled crack can reach these dimensions, then magma can follow successfully. However, owing to the permeable nature of the host rock, and the fact that the gas pressure must exceed a few MPa just to open a crack, this seems unlikely.

♦ Sills and laccoliths can grow from dikes, and dikes can grow from laccoliths and sills, because of the mechanical leverage of the large crack behind the magma front. This acts to decouple the (local) pressure gradient, driving magma into the secondary crack from the (more distant) pressure dilating that crack. In a sense, this is not much different than propagating into a previously closed portion of a dike ahead of the magma front (except that the "dike" now has a 90° bend).

5   Freezing/Remelting During Flow in a Drift

As time elapses at a given location in the flow, and temperature gradients decrease, the conductive heat flux decreases, and advection plays an increasingly important role in heat transfer. Given a sufficiently robust flow, a quasi-steady-state temperature profile develops in the thermal boundary layer adjacent to the solidification front, with cross-stream conductive heat loss being balanced by downstream advective heat input. With the temperature profile in the fluid being roughly steady at this time, the large heat flux across the boundary produces melting of the channel walls. Lister and Dellar (1996) estimated that, for flows that are much shorter than the thermal entrance length (as would be the case for flow in a drift), the distance from the source over which the initial chill has started to melt back is less than the total distance the flow has traveled by roughly the ratio of the thickness of the chilled margin that would grow by conduction in that interval, to the conduit thickness. From the results of Appendix 3.5, the flow velocity in the drifts may be taken to be of the order of that in the dike (say, 1 m/s). The thickness of the chilled margin that would grow in the time it took to fill the drift would be, from (1), only a few cm. Thus, meltback would be proceeding only over the nearest 1/100 or so of the drift, or ~ 10 m from the dike/drift intersection, at the time the drift filled. Consistent with this, the full numerical calculations carried out by Lister and Dellar for a dike thickness $2w$ of 80 cm and an initial (pre-freezing) flow velocity of 1 m/s showed that, while this dike was robust enough eventually to melt the original chill everywhere (given an unlimited source at constant pressure), in the time it took to fill the 2-km-long channel, the chilled margin still was growing everywhere. Meltback into the host rock did not occur over a significant portion of the dike until several days (~ 10^2 to 10^3 "filling" times) later.

6   Final (Frozen) Dike Thickness

It is stating the obvious to point out that the observed outcrop thicknesses of analog dikes are those that are frozen in, but it is worth remembering that these are not necessarily the thicknesses that were active upon eruption. Numerical models of buoyant dikes show

them to ascend with small-to-moderate values of the excess pressure, such that the driving pressure gradient for flow is essentially $(\Delta\rho g)' \equiv (\rho_m g - d\sigma_0 / dz)$. (Larger pressures would imply both larger thicknesses and larger pressure gradients for flow at still shallower depth, which, together, would imply fluxes too large to be fed by the supply from below.) In the tectonic environment of the Basin and Range, "buoyant" magmas must be bubble-rich. Observations of frozen, bubble-poor analog dikes suggest that these dikes may have ascended as bubble-rich but later degassed or were filled by degassed magma. If so, this filling is likely to have been associated with a substantial increase in thickness, as the excess pressure in a static column of dense magma in a region undergoing tectonic extension would increase at a rate of 10 MPa/km or more.

APPENDIX 3.5   MAGMA ASCENT IN A DIKE THAT HAS INTERSECTED THE DRIFTS

In this Appendix, we derive analytic solutions to simplified model problems intended to provide insight into the continued ascent of magma in a dike that has breached several drifts, assuming that the flow takes the form of a lava flow rather than a pyroclastic flow. The goal is not to provide the final word on this topic, as existing numerical codes can be tailored with little difficulty to provide more accurate results. Instead, this analysis is presented to justify some of the conclusions of Chapter 3, Section 3.3.3.3, regarding the height of magma in the dike at the time the drifts fill, as this work provided the basis for those conclusions.

We focus on the portion of the dike near the proposed repository; magma ascent in more distant regions of the dike will be less affected. On the basis of the results summarized in Chapter 3, Section 3.2, we assume that the dike tip has already propagated beyond the drifts when magma first reaches the drifts. The magma is treated as an incompressible fluid and the dike as a rigid vertical slot of constant thickness $2w$. Horizontal 5.5-m diameter holes (radius a) with a spacing d of 80 m are drilled into the dike. The dike is fed at depth by a fixed flux per unit length. It is assumed that the rock is sufficiently permeable that there is an atmospheric-pressure boundary condition at the flow front in both the dike and the drifts. We note in passing that if this pressure is not atmospheric (e.g., if the host rock permeability is significantly reduced by the prior influx of pyroclastic material) but is equal at the two different flow fronts, the approximate analysis to follow essentially remains unchanged; if the pressure is greater than atmospheric in the drifts but atmospheric in the dike (e.g., because the dike fracture has breached the surface), then the following analysis underestimates the height of magma in the dike at the time the drifts fill. Neglect of any elastic narrowing of the dike at the dike/drift intersection (due to locally lower pressure) will also lead to underestimates of the height of magma at the time the drifts fill, but mechanical erosion of the dike/drift intersection may to some extent counteract this.

When magma first reaches the drifts, influx is limited to that rising from directly below. As the magma level between two drifts rises to height H above the drifts, an increasing pressure gradient of order $\rho g H/(d/2)$ drives lateral flow into the drifts, and each intersected drift captures an increasing fraction of the dike flow over a width $d/2$ to each side As H increases, the flow fronts in the dike to either side of the drift may merge in the host rock directly above the drift; the drift at the dike/drift intersection may fill to the ceiling at this or some later time. Once the drift fills at the dike/drift intersection, the flow in the drift may be divided into two regions: a filled section of length L_d , where the pressure gradient for flow is P/L_d (where P is the pressure at the dike/drift intersection), and a sloping flow front region of length L_f , where the pressure gradient for flow is of the order of $2a\rho g/L_f$. As L_d increases from zero, the pressure drop in the drift offers increasing resistance to flow. For infinitely long drifts and an infinitely tall dike, H and L_d increase for all time. In the case of the proposed repository, either the drift ends or the Earth's surface will be reached first.

Solving this time-dependent problem is made difficult by the 2D nature of the flow (in the plane of the dike). To derive approximate analytic solutions, we further assume that H is sufficiently large compared to $d/2$ that treating the flow into the drifts as radially symmetric is an adequate approximation, and search for steady-state (large time) solutions. We begin by writing expressions for the magma fluxes up the dike well below the drifts (Eq. 1), from the dike into the drifts (Eq. 3), and down the drifts (Eq. 4).

Well below the drifts, the (half-)flux up the dike out to an along-strike distance $d/2$ to each side of a drift is

$$q_1 = \frac{d}{3\eta} \, w^3 \left(\Delta\rho g \right)' \tag{1}$$

where $(\Delta\rho g)'$ should be interpreted as the pressure gradient in excess of ρg that drives vertical flow. (ρ is the magma density.) A reasonable estimate of $(\Delta\rho g)'$ might be $\Delta\rho g$, but we write the expression as primed because this need not be the case.

Once H approaches ~ $d/2$, it seems reasonable to approximate the flow into the drifts as radial, with pressure boundary conditions of ρgH at a distance $d/2$ and P at a distance a from the symmetry axis. For radial symmetry, pressure p as a function of distance r from the drift center satisfies

$$\frac{d^2 p}{dr^2} = -\frac{1}{r}\frac{dp}{dr} \tag{2}$$

Solving this equation for boundary conditions of a pressure ρgH at $r = d/2$ and P at $r = a = d/29$, the pressure gradient at $r = a$ is found to be ~ $5.3(\rho gH{-}P)/(d/2)$, so the flux into the drift is

$$q_2 \approx \frac{2\pi a}{3\eta}\, w^3\, 5.3\, \frac{\rho gH - P}{d/2} \tag{3}$$

The flux down a drift is given by

$$q_3 = \frac{\pi}{8\eta}\left(c_1 a\right)^4 \frac{P}{L_d} \tag{4}$$

where $c_1 a$ should be interpreted as an "effective" radius to account for canisters or other obstructions in the drifts. (The constant c_1 may easily be determined numerically if one ignores complications due to a deforming drip shield.)

With H, P, and L_d treated as unknowns, even this model problem resists simple analytic solutions. However, useful insight can be gained by examining the end-member cases of $P \ll \rho gH$ and $P \sim \rho gH$. (The conditions under which these end-members are approached are indicated by Eq. (9) below.) For $P \ll \rho gH$, most of the pressure drop to atmospheric occurs within the dike rather than the drifts, and H approaches a limiting value as the drifts siphon off essentially 100% of the dike flow. Setting the flux up the dike, q_1 (Eq. 1), equal to the flux into the drifts, q_2 (Eq. 3) yields

$$\frac{H}{d/2} \approx 0.9 \frac{(\Delta\rho g)'}{\rho g} \tag{5}$$

where we have substituted the value of 29 for d/a.

Equation (5) states that H increases with the pressure gradient driving vertical flow $(\Delta\rho g)'$ and decreases with the weight per unit height ρg of the overlying column of magma. The value of $(\Delta\rho g)'/\rho g$ is not well constrained. A reasonable upper bound may come from assuming 1D vertical flow within a constant-thickness dike, driven by the un-vesiculated density contrast, $\Delta\rho_o$, at great depth. In this case, $(\Delta\rho g)' \sim \Delta\rho_o g(1-\theta)^{-1}$, where θ is the local bubble fraction and the factor $(1-\theta)^{-1}$ accounts for the increased vertical flow velocity required to satisfy mass balance. The parameter ρg may be written $(1-\theta)\rho_o g$, where ρ_o is the unvesiculated magma density. For $\Delta\rho_o g = 3$ MPa/km and $\rho_o g = 26$ MPa/km, $(\Delta\rho g)'/\rho g$ varies from 0.2 to 1.3 for θ varying from 0.3 to 0.7. Some-what larger values would result if θ increases with height above the drifts (reducing the effective ρg while leaving $(\Delta\rho g)'$ unchanged). However, it is more likely that $(\Delta\rho g)'/\rho g \approx 1$ is an upper bound, because (1) the likelihood of a strong component of lateral flow at shallow depth in the dike (Rubin, 2003) reduces the vertical velocity relative to the 1D vertical flow assumption, and (2) if the dike widens near the surface because of the near-universal reduction in elastic stiffness of the host rock at shallow depth (say, by a factor of M), then, from Eq. (1), $(\Delta\rho g)'$ will be reduced by a factor of M^3 relative to the estimate derived from mass balance assuming 1D vertical flow in a constant-thickness dike. This might place a "best guess" estimate of $(\Delta\rho g)'/\rho g$ near 0.1, with reasonably confident limits being 0.01 to 1. At the upper end of this range, the drifts will fill with $H \approx d/2$. At the lower end, the drifts apparently fill when $H \ll d/2$. However, when $H \ll d/2$, the assumption of radial flow is not valid and overestimates the flux into the drifts, so that H will exceed the estimate from (5). A robust conclusion is that when most of the pressure drop from $\rho g H$ to atmospheric occurs within the dike ($P \ll \rho g H$), the drifts

fill when the magma in the dike has progressed only a small fraction of the distance to the surface ($H < d/2$).

For the other end member, $P \sim \rho g H$, most of the pressure drop to atmospheric occurs within the drifts rather than the dike. In this case, a steady-state solution has the drifts siphoning off a constant fraction, C_1, of the dike flow. Setting q_3 in (4) equal to $C_1 q_1$ in (1) yields

$$\frac{\pi}{8\eta} \left(c_1 a\right)^4 \frac{\rho g H}{L_d} = C_1 \frac{d}{3\eta} w^3 \left(\Delta \rho g\right)'$$
(6)

Because the drifts capture a constant fraction of the flow, both L_d and H increase linearly with time. Then mass balance dictates

$$\frac{C_1}{1 - C_1} = \frac{\pi \left(c_2 a\right)^2 L_d}{dw\, H}$$
(7)

where the constant c_2 accounts for the average surface area in a drift cross-section taken up by canisters or other objects. Combining (6) and (7) yields a quadratic equation for C_1 leading to

$$C_1 = \frac{-1 + \sqrt{1 + 4A}}{2A} \quad , \quad A \equiv \frac{8}{3\pi^2} \frac{d^2 w^4}{\left(c_1 a\right)^4 \left(c_2 a\right)^2} \frac{\left(\Delta \rho g\right)'}{\rho g}$$
(8)

which, for $w > \sim 0.5a$, may be adequately approximated by $C_1 \approx A^{-1/2}$ (for $[\Delta \rho g]'/\rho g \approx 0.1$). Thus, for $w/a = 1$, $C_1 \approx 0.12$, and nearly all of the flow continues up the dike; for $w/a = 0.5$, $C_1 \approx 0.38$; for a "median" analog dike thickness of 1.8 m ($w/a = 0.33$), $C_1 \approx 0.65$, and the drifts capture nearly two-thirds of the dike flow. (All of these numbers are for $[\Delta \rho g]'/\rho g = 0.1$). Substituting these values of w/a and C_1 into (7) yields $H/L_d = 0.64$ for $w/a = 1$, $H/L_d = 0.28$ for $w/a = 0.5$, and $H/L_d = 0.14$ for $w/a = 0.33$. For a repository depth of 200 m to 300 m, these results imply that, for $w/a < \sim 0.5$ (a 2.75-m-

wide dike), the drifts fill before magma breaches the surface, but, for larger values, magma may breach the surface first (although the drifts would fill shortly thereafter).

To determine the conditions under which the approximations $P \sim \rho g H$ and $P << \rho g H$ are valid, set the flux from the dike into the drift (q_2 in 3) equal to the flux down the drift (q_3 in 4), yielding

$$\frac{P}{\rho g H - P} \approx 2 \frac{L_d w^3}{(c_1 a)^4} \tag{9}$$

When this ratio is much less than 1, most of the pressure drop occurs within the dike, and Eq. (5) is valid; when it is much larger than 1, most of the pressure drop occurs within the drifts, and Eqs. (7) and (8) are valid. Note that L_d appears in the numerator, so that sufficiently long drifts ultimately dominate the pressure drop, and Eqs. (7) and (8) apply. The relevant question is whether this occurs before the drifts fill. Substituting 500 m for L_d, 2.75 for a, and 0.8 for c_1 (c_1 should be refined numerically), the equality sign in (9) holds for $w \approx 30$ cm (a 60-cm dike). This is near the low end of observed thicknesses, so much thinner dikes would seem to be a low-probability event. Because of the dependence on w^3, dikes that are only modestly thicker (even less than the median thickness of 1.8 m) would satisfy $P \sim \rho g H$ for $L_d < 500$ m. Thus, the ($P \sim \rho g H$) end-member appears more appropriate for analog dikes (with the caveat that all such dikes must pass through an early phase where L_d is small and $P << \rho g H$).

Given these results, we note the following.

1. From (8), for wide dikes, the fraction of the flow captured by the drifts decreases as $(a/w)^2$ and $[(\Delta \rho g)'/\rho g]^{1/2}$. From (7), for wide dikes, the ratio H/L_d increases as $(w/a)^3$. For dikes of more moderate thickness, these "rules-of-thumb" become less accurate, but the super-linear dependence upon (w/a) persists. Thus, we expect that, for dikes somewhat narrower to somewhat thicker than the median analog dike,

H might vary from only a small fraction to a large fraction of the distance from the repository to the surface by the time the drifts fill.

2. If the dike and drifts are not orthogonal, Eqs. (7) and (8) are modified trivially by substituting $d/\sin(\theta)$ for d, where θ is the angle of dike/drift intersection.

3. Any error associated with the assumption of radial flow into the drift is unimportant if, as seems to be the case, most of the pressure drop to atmospheric occurs within the drift rather than the dike. The same may be said of the neglect of any elastic narrowing of the dike in the vicinity of the dike/drift intersection, although, in the time-dependent problem, such narrowing may increase the time required for this approximation to be accurate (that is, for most of the pressure drop to occur in the drift).

4. Because H increases linearly with L_d (once L_d becomes sufficiently large), P increases linearly with L_d, and the pressure distribution within the drift in the reference frame of the moving flow front is invariant in time. This minimizes the tendency for gas exsolution and compressibility effects (The "average" parcel of magma does not change pressure as it flows down the drift.) However, time-dependent numerical solutions may be required to determine whether such states actually are reached before the drifts fill with magma.

It may also be of interest to determine the length, L_f, of the sloping flow front in the drifts. For sufficiently slow influx, the flow front might reach the drift end before the drifts fill to the ceiling at the dike/drift intersection, and P would remain zero until the drifts filled. However, this would require an unusually thin dike. Based on the discussion following (9), to make a rough estimate of L_f, we assume $P \sim \rho g H$. Then the flow

velocity in the drift is constant and, from (7), the pressure gradient within the filled section of drift is

$$\frac{\rho g H}{L_d} = \frac{1 - C_1}{C_1} \frac{\pi \left(c_2 a\right)^2}{dw} \rho g \tag{10}$$

Because the flow velocity is constant in this steady-state solution, L_f is also constant, and the velocity within the flow front is the same as that within the filled section of drift. An upper bound on L_f can be derived from the assumption that the "global" pressure gradient, $\rho g(2a)/L_f$, within the flow front is equal to the pressure gradient, $\rho g H/L_d$, within the filled section of drift. (This is an upper bound because the flow front profile is expected to be convex upward rather than linear, owing to the greater resistance to flow near the thin leading toe.) Setting $\rho g(2a)/L_f$ equal to the right side of (10) yields

$$\frac{L_f}{d} = \frac{2}{c_2^2 \pi} \frac{C_1}{1 - C_1} \frac{w}{a} \tag{11}$$

For the median dike thickness of $w/a = 0.33$ (so $C_1 \approx 0.65$ for $(\Delta\rho g)'/\rho g \approx 0.1$), (11) indicates an upper bound on L_f of ~ 40 m.

APPENDIX 3.6   FACTORS INFLUENCING THE STRESS STATE AT THE REPOSITORY AND THE LIKELY ORIENTATIONS OF SECONDARY FRACTURES EMANATING FROM THE DRIFTS

Topography

The surface elevation above the ends of the drift is as much as 100 m below that of the highest point. Assuming a linear increase of stress with depth, this could result in a reduction of the least compressive stress at repository depths of roughly 1 MPa, relative to that acting beneath the topographic high.

Stresses Due to the Drift

These may be produced by tunneling (removal of load-bearing rock), thermal loading, pressurization by magma, and the presence of the drift in the face of the dike-induced stress perturbations listed below. Away from the drift ends, these stresses are fairly straightforward to compute. (In the case of the drift-induced modification of the dike-induced stresses it is sufficient to (1) compute the dike-induced stresses in the absence of the drift, and then (2) impose the stresses acting along the drift axis as the far-field boundary conditions surrounding a stress-free hole). However, the mechanical influence of the end of the drift, and the uneven thermal loading at this point, may produce stresses that are quite different from, and possibly less compressive than, those away from the ends. Stresses near the drift ends must be computed numerically (i.e., from 3D finite element models).

Dike-Induced Stresses

Immediately adjacent to the dike, the normal stress on dike-parallel fractures is equal to the pressure in the dike (so the change in stress is equal to the dike pressure minus the pre-existing stress on the dike plane). With increasing distance (but less than the dike length), the host rock "sees" an average of the stress change over a larger and larger portion of the dike. At distances comparable to the dike length or greater, the rock sees just

the elastic effect of the dike opening, and details of the loading distribution are lost. This makes for a range of possible stress changes at repository depths. Near the dike the stress change could be tensile (if the dike is filled by pyroclastic material at near-atmospheric pressure) or compressive (if the dike is filled by dense magma or a pyroclastic flow under choked conditions). Tensile stresses on dike-parallel planes are produced to depths somewhat below the dike top before the dike breaches the surface (Rubin and Pollard, 1988), and, in map view, off to the side and somewhat behind the tip of a dike of finite lateral extent. The latter implies that if a dike a few kilometers long ends within the repository footprint, a few drifts intersected by the dike might be subjected to tensile stress perturbations that are a modest fraction of the dike excess pressure, hundreds of meters from the parent dike.

Stresses Due to Dike-Induced Fault Slip

Earthquakes are ubiquitous during dike propagation. Historically, in any particular tectonic setting, the maximum size of the earthquakes accompanying intrusion tends to increase with elapsed time since the last intrusion, reaching magnitude 5.5-6 in some cases in Iceland (Rubin and Gillard, 1998). This is consistent with the notion that tectonic extension between intrusions tends to bring the rock closer to failure, while intrusion generally increases the horizontal stress and moves the rock farther from failure (adjacent to but not beyond the ends of the intrusion). Given that the stress state at Yucca Mountain resides near the failure envelope (Stock et al., 1985), normal faulting is virtually certain to occur in conjunction with a propagating dike. Such faulting might be suppressed locally at depths near the proposed repository because of increased horizontal thermal stresses, but not at greater or lesser depths. As earthquakes themselves are not expected to present much hazard, the biggest influence of such normal faulting might lie in how it affects dike propagation. Horizontal stress changes in conjunction with normal faulting are spatially variable, but, in most regions adjacent to the fault, they are compressive (locally, they are tensile); on the length scale of the fault, they are of the order of the fault stress drop. Thus, induced normal faulting is an additional mechanism that could reduce the lag zone length. Because the largest normal faults at Yucca Mountain

have been mapped, the range of stress changes they produce upon slip can be evaluated sensibly using 2D and 3D elastic models.

Stresses Due to Dike-Induced Tensile Fracturing

Paired tensile cracks or crack sets often are observed to occur parallel to and symmetrically about an eruptive fissure, or to diverge from the ends of an eruptive fissure (Pollard et al., 1983; Mastin and Pollard, 1988). These cracks are inferred to grow down from the surface at maxima in the dike-induced horizontal tensile stress. Numerical and experimental studies indicate that the depth of the dike top at the time of crack formation might be half (or more) of the separation between the crack sets for a quasi-uniform excess magma pressure, but 1/4 to 1/5 the separation between the crack sets for a magma pressure distribution more appropriate for lateral dike propagation (Rubin, 2003). The largest system of paired crack sets of which we are aware surround an eruptive fissure in the King's Bowl lava field on the Snake River Plain (Greeley et al., 1997). These crack sets are separated by ~ 1.6 km, suggesting that the dike top might have been more than 300 m deep when they formed. If comparable fissures at Yucca Mountain could grow to depths approaching 200m to 300 m, they may significantly reduce the compressive stress acting across potential secondary dog-leg fractures distant from the parent dike. The depth to which such fractures might extend can be estimated using 2D and 3D boundary element models. 2D calculations that are rather favorable for crack growth — in that (a) the fracture toughness is assumed to be zero, and (b) the cracks are assumed to initiate just before the dike tip goes unstable — show that such cracks might grow to a 160 m depth a few hundred meters from the dike plane. 3D calculations for a 2 km dike reduce this to 130 m. While a larger variety of calculations can be carried out, at present, it seems unlikely that such cracks would grow to repository depths (for more details see Rubin, 2003).

 Influence of the Stress State on the Orientation of Secondary Active Fracture

In this section, we examine various scenarios of magma breaking out of the drifts, once the repository has been pressurized by magmatic material. The requirements for this breakout are discussed in the main Report and other Appendices; here, we assume that such breakout occurs and consider only the likely orientations of the resultant fractures. We consider separately two situations: Case 1, where the horizontal stresses are larger than the vertical stress; and Case 2, where the vertical stress remains the maximum compressive stress. (Note that the horizontal and vertical stresses are contrasted at the repository scale, not at the drift scale.)

Case 1 (Horizontal Stresses are Larger than the Vertical Stress)

This situation arises within the period spanning approximately a few hundred years to a few thousand years following closure of the repository, in the hot design scheme. To the first order, the pressure in the drift system will be equal to the horizontal stress perpendicular to the dike (i.e., the original in-situ stress augmented by the thermal component). Under these conditions, the drifts would more likely break at mid-height, and a system of horizontal fractures (which could possibly link) would form. In effect, this magma eruption from the drifts would lead to the propagation of sills. Outside the repository area, where the vertical stress again becomes the major compressive stress, the magma-filled fracture would either progressively reorient to eventually propagate along vertical planes perpendicular to minimum horizontal stress or feed magma into pre-existing vertical fractures. (Reorientation of the fractures would be accompanied by multiple break-ups of the crack edge, associated with mode-III fracture propagation.) Note, however, that a significant volume of magma could be held inside the sill, especially when accounting for the increased storage due to bulging of the ground surface, for crack radius to depth ratio exceeding 1. Therefore, calculations should be performed to assess the possibility that the system of drifts and the sills (within the repository footprint) could contain the volume of magma diverted from the main dike. The model of a penny-shaped crack parallel to the free surface (Zhang et al., 2003) can be used to compute the radius of a sill in

stable limit equilibrium (i.e., no further propagation takes place), given the volume of magma it contains, the elastic properties of the rock and its toughness.

Case 2 (Vertical Stress Remains the Maximum Compressive Stress)

We consider two mechanisms of magma breakthroughs:

> *Case 2a* — The magma erupts along fractures aligned with the drift axis that have initiated in the crown and in the floor of the tunnel; and

> *Case 2b* — The magma erupts along pre-existing fractures that are sub-orthogonal to the drift (and, thus, roughly parallel to the dike plane).

Case 2a — This case is plausible, as, in the absence of thermal stresses and when the tunnels are not pressurized, the stress concentration around the drifts yields low values of the hoop stress in the crown and in the floor. However, propagation of the fractures beyond a distance approximately equal to the drift diameter causes the fracture to be orthogonal to the smallest horizontal stress. The energy losses associated with fracture turning imply that these fractures are unlikely to propagate far beyond the zone of stress concentration. Thus, in this scenario, we can conclude that the magma would erupt along the original dike, even though vertical longitudinal fractures would have initiated along the drifts.

Case 2b — We consider the simplified scenario of an existing fracture parallel to the dike. It is expected that the aperture of this fracture would be less than the opening of the dike under most circumstances, as it closed by compressive stress. Although one would infer from static considerations alone that the pre-existing fracture would reopen, because the magma pressure in the drift is about the same as the normal stress across the fracture, it is easy to argue using hydrodynamical considerations that most of the magma would flow in the fracture with the widest opening — i.e., along the pre-existing dike in this case. Nonetheless, eruption of magma along this existing fracture rather than the dike

cannot be ruled out entirely, owing to the possible sources of tensile stress perturbations discussed earlier in this Appendix.

In summary, if the horizontal stress is more compressive than the vertical stress (approximately during the first few thousands years following sealing of the repository, in the hot design), the magma would escape the drifts via the formation of sills. If the sill extends into the region outside the repository where the vertical stress is again the maximum compressive stress, then the possibility exists that the magma could reach the surface, either by pre-existing vertical fracture or by reorientation of the initially horizontal fracture. If the horizontal stress is less compressive than the vertical stress, the magma would preferentially erupt along the original dike, but it is possible to imagine scenarios where the normal stresses acting across pre-existing vertical fractures intersecting the drifts would be favorable for their dilation as well.

APPENDIX 3.7   OBSTRUCTIONS OF THE PARENT DIKE AND THEIR INFLUENCE ON DOG-LEG PROBABILITIES

High pressures at the dike/drift intersection seem easiest to achieve if the parent dike or vent has been obstructed in some way. Possibilities include normal faulting of a hanging-wall block into the dike tip cavity or freezing of previously emplaced magma. In addition to those scenarios that might cause blockage in the absence of a repository, if the parent dike is thin enough to be susceptible to freezing in any case (see Appendix 3.4), then siphoning off of a large fraction of the flow by the drifts could promote freezing of the parent dike above the level of the drifts (see Appendix 3.5).

Whatever the cause, an obstruction in the parent dike removes a potential "pressure-release valve" from the system and might allow the pressure at the dike/drift intersection to increase. In this case, it is important for TSPA purposes to determine which fails first in response to this pressure increase: the drift (in the form of a dog-leg fracture), or the obstruction? We consider magma flows and pyroclastic flows separately below.

1   Magma Flows

Once the magma front stops, the pressure at the level of still-liquid magma below may increase as a result of the continued ascent of buoyant magma or bubbles. The maximum pressure that may be attained (prior to failure of the system) is limited not by the dike-normal stress or the weight of the overlying column of magma but by the degree of magma or bubble ascent. (For a discussion of pressure increases due to bubble ascent, see Linde et al., 1994).

Dike Blocked By Normal Faulting: In the absence of thermal stresses, normal faulting is expected to occur preferentially at shallow depth where the stress perturbation due to the dike is high but the confining pressure low. With horizontal thermal stresses reaching 5MPa to 10 MPa, the tendency for normal faulting at the repository level is decreased substantially (Rubin and Gillard, 1998), but normal faulting above the level of the large horizontal thermal stresses is not.

To address the question of whether flow continues up the dike (via either the fault or a planar extension of the dike) or via a dog-leg fracture as the magma pressure increases, one must consider both the magma pressure at the site of the potential fracture and the normal stress acting across that fracture. By supposition, the magma front in the dike has been halted; to achieve large pressures in the drift distant from the parent dike, the drift must be filled. In this case, the magma pressure distribution essentially is hydrostatic, and the pressure at the dike/fault intersection is less than that in the drift by $\rho_m gH$, where *H* is the height of the obstructing fault above the repository.

Factors controlling the normal stress are much more numerous. The normal stresses acting across potential dog-leg fractures are influenced by many sources, including topography, dike-induced stresses, and natural variability (see Appendix 3.6 and Chapter 3, Section 3.4.2 of the main Report). While most of these are not expected to produce stress variations exceeding ~ 1 MPa, compressive thermal stresses of several MPa are expected for most of the first 10,000 years of the life of the repository. Because such stresses inhibit normal faulting, they are likely to be absent or much reduced at the dike/fault intersection.

Normal stresses acting at the dike/fault intersection (across either the fault or the extension of the dike) are also influenced by several factors. To the extent that the dike/fault intersection is shallower than the potential dog-leg fracture, the overburden-induced stresses can be expected to be lower. The most important variable is the extent to which fault slip alters the large tensile stress concentration at the dike tip. If the fault cuts both walls of the dike, such that an unbroken hangingwall extends across the dike plane, there will be a large dike-induced tensile normal stress acting on the up-dip portion of the fault that (in addition to the probable lack of large thermal stresses) will favor propagation up the fault rather than initiation of a dog-leg. This is the most likely scenario, at least at depths greater than a few tens of meters, as only a single (existing) fault is required to intersect the dike at one point. (Observations of "keystone collapse" of a wedge-shaped block into the dike cavity, to our knowledge, are restricted to near-surface exposures —

e.g., where a dike cuts a cinder cone.) The situation seemingly most favorable for a dog-leg would be if such a "keystone", or perhaps the "triangular" section of the hangingwall bounded by the free surface, the portion of the fault up-dip of the dike/fault intersection, and the dike plane, were completely unsupported by the rest of the hangingwall and rested entirely on the fault segment up-dip of the dike. In this case, the dike-induced tensile stresses essentially are relieved by fault slip, and only differences in depth/topographic stresses/fracture orientation and the presence/absence of thermal compressive stresses are available to distinguish the normal stress across the fault from that acting across a potential dog-leg fracture. The first group of stresses could favor flow up either the fault or the dog-leg, depending upon the depth of the dike/fault intersection and the buoyancy of the magma. However, the significant magnitude of the thermal stresses at repository depths, together with their probable absence or significantly reduced magnitude at the depth of the dike/fault intersection, would seem to be the most important consideration in this case and, again, favors flow up the fault rather than initiation of a dog-leg.

Dike Blocked by Freezing: We distinguish the following two types.

1. Freezing in a Thin Near-Tip Region — The considerations are much the same as for a dike blocked by faulting, except that the absence of faulting removes one mechanism for relieving the dike-induced tensile stresses. Owing to the large tensional stresses imparted by the inflating dike, renewed propagation of the parent dike seems highly favored over initiation of a dog-leg fracture.

2. Freezing in Bulk — This may inhibit renewed propagation of the parent dike, but it also inhibits the ascent of magma or bubbles driving pressurization of the parent dike. If the dike above the level of the repository is substantially frozen because the drifts have siphoned off a large fraction of the flow, the most likely outcome would seem to be continued ascent of the dike at points distant from the repository.

Cylindrical Conduit Blocked by Freezing: If this point is reached, then the parent dike presumably has long since frozen (see Appendix 3.4). If only the near-surface portion of the cylindrical conduit is frozen, then blowing out of the frozen plug seems the most likely response to a pressure increase. If most of the plug above the repository is frozen, then freezing below the repository and within the 5.5-m diameter drift appears very likely as well. Initiating new dikes off the conduit that intersect "pristine" (unfilled by magma) drifts is also possible, but this scenario resembles the original one of an unobstructed propagating dike intersecting some drifts.

2 Pyroclastic Flows

In some sense, most violent pyroclastic conduit flows are "obstructed" even while they vent to the surface. The (small) pressure drops due to viscous resistance and the density of the erupting column do not allow the flow to reach near-atmospheric pressure until after some constriction is passed (which is the end of the vent for a sufficiently straight-walled conduit). However, the existence of a vent to the surface would still lead to lower stresses at repository depths than would occur in the absence of such a vent.

Again, it seems more likely that a pyroclastic flow would circumvent a mechanical obstruction within the parent dike than form a dog-leg fracture. The reasons are much the same as those discussed in connection with magma flows above. One difference is that for a dike blocked by normal faulting, for a pyroclastic flow, there might not be a significant pressure drop from the dike/drift intersection to the obstruction, making failure of the obstruction (i.e., continued ascent of the flow either along the fault or vertically) even more highly favored relative to initiation of a dog-leg off the drift than was the case for magma flows. Another difference is that if one is considering blockage of the parent dike or vent due to freezing, one is most likely not considering a pyroclastic flow entering a pristine drift, but pressurizing a drift that is already full of partially solidified magma. This makes initiation of a dog-leg susceptible to the same "thermal death" issue as that surrounding a magmatic dog-leg (unless drainback into the dike has occurred to a depth of more than ~ 300 m).

APPENDIX 3.8   RADIAL DIFFUSION OF GAS FROM A DRIFT

The volumetric flux per square meter, u (units of m/s), for fluid flow through a porous medium is given by

$$u = -\frac{k}{\eta}\frac{dp}{dr} \tag{1}$$

where k is the matrix permeability, η is the fluid viscosity, p is the pressure, and r is distance. Note that u is essentially a "bulk" flow velocity, a factor of ϕ (the porosity) less than the actual average velocity of the fluid phase.

Under conditions of radial flow, the mass balance equation is

$$r\phi\frac{d\rho}{dt} = -\frac{d}{dr}(\rho u r) \tag{2}$$

where ρ is the gas density, and t is time. Here we have assumed that porosity, ϕ, is a constant independent of pressure, a reasonable approximation in that the gas is so much more compressible than the pore volume.

Combining (1) and (2) yields

$$\frac{dp}{dt} = \frac{k}{\eta\phi}\frac{1}{r}\frac{d}{dr}\left(pu\frac{dp}{dr}\right) \tag{3}$$

Here, we have assumed that permeability, k, and viscosity, η, are constants independent of pressure and temperature, and we have made the isothermal assumption that ρ is simply a constant times the pressure, p. Note that the assumptions of constant permeability and (at least until condensation of water vapor occurs) isothermal compressibility are conservative in that they increase the pressure required to move a given mass flux, relative to what would be expected (increasing pressure leading to perhaps greatly increased fracture permeability and decreasing temperature leading to a larger gas mass storage capacity at a given pressure). Viscosity for steam varies only from about 4 x 10^{-5} Pa s to

1 x 10^{-5} Pa s as the temperature decreases from about 800 $^{\circ}$C to 100 $^{\circ}$C and is very insensitive to pressure.

Equation (3) is solved subject to boundary conditions $p = 0.1$ MPa (1 atmosphere) far from the drift and a specified (time-varying) gas velocity, u , at the drift wall ($r = 2.75$ m). To determine this velocity boundary condition, we assume a constant mass flux of magma into the drift and use the linearity of the gas volume fraction at low pressure (see Figure 2-1c) to estimate that, for ~ 4 wt % H_2O, 1 m^3 of dense basalt corresponds to ~ 60(MPa/p) m^3 gas, where p is the pressure. For a drift radius of 2.75 m and an average length of 1.2 km, this corresponds to a velocity of (2.9 mm/s) (MPa/p) per m^3/s of dense basalt that enters the drift. To translate a mass flux into the drift into a volume flux of dense magma, we use a density of 2.5 x 10^3 kg/m^3, so (for example) a mass flux of 10^5 kg/s corresponds to a dense magma volume flux of 40 m^3/s and a gas volume flux of (2400 m^3/s) (MPa/p).

For a constant mass flux into the drift, the drift pressure gradually rises as high pressures diffuse farther into the host rock. At some time, the pressure fields of adjacent drifts overlap, and, at some (earlier or later) time, the drifts may fill with pyroclastic debris. The drift volume is ~ 2.8 x 10^4 m^3 and (assuming dense magma) would take ~ 700 s to fill at a mass flux of 10^5 kg/s and ~ 70 s to fill at a mass flux of 10^6 kg/s. (Divide these times by ~ 2 for filling with tephra). The filling time would be longer if most solids go up the dike; in this case, however, the dike must be venting to the surface, and that venting will put its own limit on the pressure at the dike/drift intersection. By imposing the gas velocity at the drift wall as a boundary condition, the time required to fill the drift with gas is neglected, but this is insignificant compared to the filling time by tephra.

The solid curves in Figure A3.8-1 show the time evolution of pressure in the drift for mass fluxes into the drift of 10^5 and 10^6 kg/s. In addition to the above values of magma density and water content, we adopt $\eta = 3 \times 10^{-5}$ Pa s (appropriate for a temperature of ~ 550 °C), $k = 10^{-12}$ m^2 (toward the low end of values measured in situ at the meter scale, but probably an underestimate at the drift scale), and $\phi = 0.1$. For these parameters, the drift pressure reaches values of ~ 2 MPa and ~ 5 MPa by the time the drifts fill for the lower and higher mass fluxes, respectively. These pressures increase to only ~ 2 MPa and ~ 6 MPa for filling times ten times larger (if, for example, 90% of the solid or liquid material goes up the dike, but all the gas appropriate for these mass fluxes goes into the drifts). The dashed curves in Figure A3.8-1 show the evolution of the pressure at a distance of 40 m from the drift axis. This pressure remains essentially atmospheric to times longer than the drift filling time, indicating that the 1D radial flow approximation is adequate.
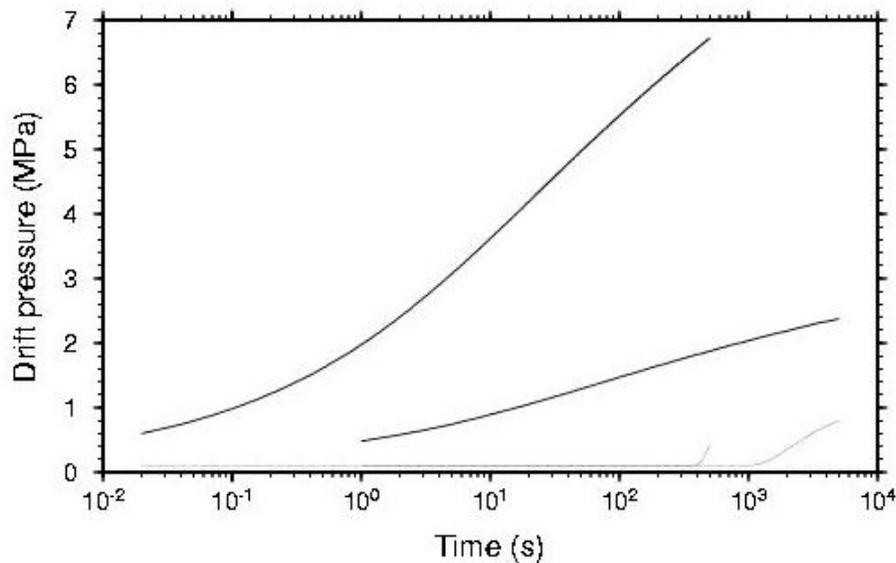

Figure A3.8-1 *(solid curves) Drift pressure as a function of time for mass fluxes into a drift of 10^6 (top) and 10^5 (bottom) kg/s (At these mass fluxes, the approximate "filling times" of the drift are ~ 40 s and 400 s, respectively); (dashed curves) The evolution of pressure at a distance of 40 m from the drift axis, corresponding to the midpoint between adjacent drifts.*

These calculations can be augmented by considering the following processes. It may be that some of these can be shown to have a negligible influence on the drift pressure without resorting to full-scale numerical calculations, but the Panel felt it was preferable to list them so that others perhaps more familiar with the processes involved could judge:

(1) the complex permeability structure of the host rock — This will probably reduce the "effective" porosity, ϕ, and thus tend to increase the computed drift pressure;

(2) the volume decrease and viscosity decrease of the water vapor as it cools — Both of these effects will decrease the computed drift pressure. The adopted viscosity is an approximate average from magmatic to the boiling temperatures. However, the volume decrease upon cooling is not included in the calculations shown in Fig A3.8-1;

(3) the condensation of vapor to water — In an approximate sense, the volume decrease compensates for the viscosity increase in that a given pressure gradient can move a larger mass flux of water than steam. However, the physics governing the storage capacity of the rocks is very different for vapor and water (gas compressibility versus pore volume compressibility and infiltration of water into unsaturated rocks). It seems likely that on balance condensation will reduce the computed drift pressure;

(4) the boiling of any pore water remaining in the heated rock in the vicinity of the drifts — This will increase the computed drift pressure, but whether the influence of this process is significant is unknown. (Certainly it will not be significant if most pore water has been driven off.);

(5) the pressure sensitivity of the permeability of the host rock at the drift scale, which is dominated by a fracture permeability that may increase

dramatically as the gas pressure approaches the normal stress — This
will act to reduce the computed drift pressure. On the other hand, be-
cause this mechanism depends upon the difference between the
fracture-normal stress and the gas pressure, by the same mechanism,
large thermal stresses in the vicinity of the drifts could act to decrease
the permeability relative to what is measured today (at low gas pres-
sure);

(6) infiltration of the host rock by fine pyroclastic material — This would
reduce the effective permeability and increase the computed drift pres-
sure. Whether this process can be significant prior to the drift filling
with pyroclastic material is unknown.

The goal of considering these processes would be to see if drift pressures approaching the
expected normal stress acting across potential dog-leg fractures can be reached. At pres-
ent, it seems that the computed pressures of < 2 MPa associated with a mass influx of
10^5 kg/s are too low to lead to a dog-leg, given even very modest thermal stresses. How-
ever, given the variability in the normal stress that one might reasonably expect,
pressures a few times larger could be significant. The pressures associated with a mass
flux of 10^6 kg/s are significant, but reaching such mass fluxes on a such a short timescale
seems unlikely. Note also that mass fluxes of 10^5 kg/s to 10^6 kg/s typically are associated
with venting to atmospheric pressure; if pressures of several MPa develop in the drift
(still too small to overcome the expected nominal thermal stresses), one might expect the
mass flux into the drift to diminish. (The relevant comparison is probably between the
pressure in the drift and the vent pressures upstream of the choking point under choked
flow conditions.)

REFERENCES

Batchelor, G. K., *An Introduction to Fluid Dynamics*, Cambridge University Press, Cambridge, 1967.

Bruce, P. M., and H. E. Huppert, Solidification and melting along dikes by the laminar flow of basaltic magma, in *Magma Transport and Storage*, edited by M. P. Ryan, pp. 87-101, Wiley, Chichester, England, 1990.

Delaney, P. T., and D. D. Pollard, *Deformation of Host Rocks and Flow of Magma During Growth of Minette Dikes and Breccia-Bearing Intrusions Near Ship Rock, New Mexico, U.S. Geological Survey*, Professional Paper, p. 61, 1981.

Delaney, P. T., and D. D. Pollard, Solidification of basaltic magma during flow in a dike, *Am. J. Sci.*, *282*, 856-885, 1982.

Detournay, E., and A. Savitski, *Mathematical Models of Propagating Dikes, Bechtel SAIC*, 2003.

Duffield, W., R. L. Christiansen, R. Y. Koyanagi, and D. W. Peterson, Storage, migration, and eruption of magma at Kilauea Volcano, Hawaii, 1971-1972, *J. Volcanol. Geotherm. Res.*, *13*, 273-307, 1982.

Erickson, L., A three-dimensional dislocation program with applications to faulting in the Earth, M.S. Thesis, Stanford University, 1986.

Fialko, Y. A., and A. M. Rubin, Thermodynamics of lateral dike propagation: Implications for crustal accretion at slow spreading mid-ocean ridges, *J. Geophys. Res.*, *103*, 2501-2514, 1998.

Foshag, W., and J. Gonzales, Birth and development of Paricutin Volcano, *USGS Bull.*, *965D*, 355-485, 1956.

Greeley, R., and E. K. Thelig, J. S., *Guide to the Geology of the King's Bowl Lava Field, in Volcanism of the Eastern Snake River Plain, Idaho: A Comparative Planetology Guidebook*, edited by R. Greeley, and J. S. King, pp. 177-188, NASA, Washington, D.C., 1977.

Hills, D., P. Kelly, D. Dai, and K. Korsunsky, *Solution of Crack Problems. The Distributed Dislocation Technique*, Solid Mechanics and Its Applications, vol. 44, Kluwer Academic Publ., Dordrecht, 1996.

Linde, A., I. S. Sacks, M. J. S. Johnston, D. P. Hill, and R. G. Bilham, Increased pressure from rising bubbles as a mechanism for remotely triggered seismicity, *Nature*, *371*, 408-410, 1994.

Lister, J. R., Buoyancy-driven fluid fracture: The effects of material toughness and of low-viscosity precursors, *J. Fluid Mech.*, *210*, 263-280, 1990.

Lister, J. R., The solidification of buoyancy-driven flow in a flexible-walled channel. Part 1. Constant-volume release, *J. Fluid Mech.*, *272*, 21-44, 1994.

Lister, J. R., and P. J. Dellar, Solidification of pressure-driven flow in a finite rigid channel with application to volcanic eruptions, *J. Fluid Mech.*, *323*, 267-283, 1996.

Lister, J. R., and R. C. Kerr, Fluid-mechanical models of dike propagation and their application to magma transport in dykes, *J. Geophys. Res.*, *96*, 10,049-10,077, 1991.

Mastin, L. G., and D. D. Pollard, Surface deformation and shallow dike intrusion processes at Inyo Craters, Long Valley, California, *J. Geophys. Res.*, *93*, 13,221-13,236, 1988.

Melnik, O., Dynamics of two-phase conduit flow of high-viscosity gas-saturated magma: Large variations of sustained explosive eruption intensity, *Bull. Volcanol.*, *62*, 153-170, 2000.

Okada, Y., Internal deformation due to shear and tensile faults in a half-space, *Bull. Seism. Soc. Am.*, *82*, 1018-1040, 1992.

Pollard, D. D., P. T. Delaney, W. A. Duffield, E. T. Endo, and A. Okamura, Surface deformation in volcanic rift zones, *Tectonophysics*, *94*, 541-584, 1983.

Rice, J. R., Mathematical analysis in the mechanics of fracture, in *Fracture, An Advanced Treatise*, vol. II, Ch. 3, edited by H. Liebowitz, pp. 191-311, Academic Press, New York, 1968.

Rubin, A. M., A comparison of rift-zone tectonics in Iceland and Hawaii, *Bull. Volcanol.*, *52*, 302-319, 1990.

Rubin, A. M., Propagation of magma-filled cracks, *Ann. Rev. Earth Planet. Sci.*, *23*, 287-336, 1995a.

Rubin, A. M., Getting granite dikes out of the source region, *J. Geophys. Res.*, *100*, 5911-5929, 1995b.

Rubin, A. M., *Background Report on Dike Propagation, Bechtel SAIC*, 2003.

Rubin, A. M., and D. Gillard, Dike-induced earthquakes: Theoretical considerations, *J. Geophys. Res.*, *103*, 10,017-10,030, 1998.

Rubin, A. M., and D. D. Pollard, Dike-induced faulting in rift zones of Iceland and Afar, *Geology*, *16*, 413-417, 1988.

Stock, J. M., J. H. Healy, S. H. Hickman, and M. D. Zoback, Hydraulic fracturing stress measurements at Yucca Mountain, Nevada, and relationship to the regional stress field, *J. Geophys. Res.*, *90*, 8691-8706, 1985.

Tada, H., P. C. Paris, and G. R. Irwin, *The Stress Analysis of Cracks Handbook*, Del Research Corp., St. Louis, 1985.

Turcotte, D. L., and G. Schubert, *Geodynamics*, Wiley, Chichester, England, 1982.

Wang, K., T. Plank, J. D. Walker, and E. I. Smith, A mantle melting profile across the Basin and Range, southwestern USA, *J. Geophys. Res.*, *107*, DOI 10.1029/2001JB000209, 2002.

Zhang, X., E. Detournay, and R. Jeffrey, Propagation of a penny-shaped hydraulic fracture parallel to the free-surface of an elastic half-space, *Int. J. Fracture*, *115*, 125-158, 2002.